Publication Year	2021
Acceptance in OA	2022-09-08T15:48:16Z
Title	The Dark World: A Tale of WASP-43b in Reflected Light with HST WFC3/UVIS
Authors	Fraine, Jonathan, Mayorga, L. C., Stevenson, Kevin B., Lewis, Nikole K., Kataria, Tiffany, Bean, Jacob L., BRUNO, GIOVANNI, Fortney, Jonathan J., Kreidberg, Laura, Morley, Caroline V., Mouawad, Nelly C., Todorov, Kamen O., Parmentier, Vivien, Wakeford, Hannah, Feng, Y. Katherina, Kilpatrick, Brian M., Line, Michael R.
Publisher's version (DOI)	10.3847/1538-3881/abe8d6
Handle	http://hdl.handle.net/20.500.12386/32558
Journal	THE ASTRONOMICAL JOURNAL
Volume	161

The Astronomical Journal, 161:269 (20pp), 2021 June https://doi.org/10.3847/1538-3881/abe8d6

The Dark World: A Tale of WASP-43b in Reflected Light with HST WFC3/UVIS

Jonathan Fraine[1,2], L. C. Mayorga[3,4], Kevin B. Stevenson[4], Nikole K. Lewis[5], Tiffany Kataria[6], Jacob L. Bean[7], Giovanni Bruno[8], Jonathan J. Fortney[9,10], Laura Kreidberg[3,11], Caroline V. Morley[12], Nelly C Mouawad[13], Kamen O. Todorov[14], Vivien Parmentier[15], Hannah Wakeford[16], Y. Katherina Feng[9,10,19], Brian M. Kilpatrick[17], and Michael R. Line[18]

[1] Space Science Institute Center for Data Science, USA
[2] Space Science Institute Center for Exoplanet and Planetary Science, USA
[3] Center for Astrophysics | Harvard & Smithsonian, 60 Garden Street, Cambridge, MA 02138, USA
[4] Johns Hopkins APL, 11100 Johns Hopkins Road, Laurel, MD 20723, USA
[5] Department of Astronomy and Carl Sagan Institute, Cornell University, 122 Sciences Drive, Ithaca, NY 14853, USA
[6] California Institute of Technology–Jet Propulsion Laboratory, USA
[7] University of Chicago Department of Astronomy and Astrophysics, USA
[8] INAF–Catania Astrophysical Observatory, Via Santa Sofia, 78, I-95123 Catania, Italy
[9] Department of Astronomy & Astrophysics, University of California, USA
[10] University of California, Santa Cruz, Other Worlds Laboratory, USA
[11] Max Planck Institute for Astronomy, Königstuhl 17, 69117, Heidelberg, Germany
[12] University of Texas at Austin College of Natural Sciences, USA
[13] Lebanese American University Department of Natural Science, USA
[14] University of Amsterdam Anton Pannekoek Institute for Astronomy, The Netherlands
[15] University of Oxford Department of Physics, UK
[16] School of Physics, University of Bristol, HH Wills Physics Laboratory, Tyndall Avenue, Bristol BS8 1TL, UK
[17] Space Telescope Science Institute, USA
[18] Arizona State University, School of Earth and Space Exploration, USA

Received 2020 April 7; revised 2020 December 12; accepted 2020 December 14; published 2021 May 19

Abstract

Optical reflected light eclipse observations provide a direct probe of exoplanet scattering properties, such as from aerosols. We present here the photometric reflected light observations of WASP-43b using the Hubble Space Telescope (HST) WFC3/UVIS instrument with the F350LP filter (346–822 nm) encompassing the entire optical band. This is the first reflected light photometric eclipse using UVIS in scanning mode; as such, we further detail our scanning extraction and analysis pipeline `Arctor`. Our HST WFC3/UVIS eclipse light curve for WASP-43b derived a 3σ upper limit of 67 ppm on the eclipse depth, which implies that WASP-43b has a very dark dayside atmosphere. With our atmospheric modeling campaign, we compared our reflected light constraints with predictions from global circulation and cloud models benchmarked with HST and Spitzer observations of WASP-43b. We infer that we do not detect clouds on the dayside within the pressure levels probed by HST WFC3/UVIS with the F350LP filter ($P > 1$ bar). This is consistent with the general circulation model predictions based on previous WASP-43b observations. Dayside emission spectroscopy results from WASP-43b with HST and Spitzer observations are likely to not be significantly affected by contributions from cloud particles.

Unified Astronomy Thesaurus concepts: Exoplanet atmospheric composition (2021); Exoplanet atmospheres (487); Exoplanet astronomy (486); Exoplanets (498); Atmospheric composition (2120); Atmospheric science (116); Planetary atmospheres (1244)

Supporting material: data behind figure

1. Introduction

The climates of planets in the solar system and beyond are strongly shaped by the presence of aerosols (clouds and/or hazes) in their atmospheres. These clouds and hazes can reflect starlight back into space, absorb photons from across the stellar spectrum, and emit at longer wavelengths (Marley et al. 1999; Sudarsky et al. 2000). Because aerosols are expected to efficiently reflect starlight into space, aerosol properties can be constrained through planetary optical and near-ultraviolet (NUV) reflection spectra, often called albedo spectra. Optical/NUV observations of solar system objects are abundant, but only a handful of exoplanets have been measured in reflected light (Evans et al. 2013; Heng & Demory 2013; Angerhausen et al. 2015; Esteves et al. 2015; Shporer & Hu 2015; Haggard & Cowan 2018; Jansen & Kipping 2018).

Transiting exoplanet eclipse observations provide a method for direct detection of photons from an exoplanet's atmosphere. Eclipse measurements derive the dayside brightness of the exoplanetary atmosphere, which in the optical and NUV provides a measure of the geometric albedo of the planet. From such measurements, we can infer the compositions of the materials (clouds, hazes, molecules, and atoms) that most strongly shape the albedo spectrum of the planet (Marley et al. 1999).

To date, the presence of aerosols in exoplanetary atmospheres has largely been inferred through the muting of molecular spectroscopic features at infrared wavelengths and scattering slopes, or lack thereof, at visible wavelengths seen in transmission spectra (e.g., Esteves et al. 2015; Nikolov et al. 2015; Nortmann et al. 2016, 2018; Sing et al. 2016; Allart et al. 2017, 2019; Chen et al. 2017a, 2017b, 2018, 2020; Palle et al. 2017; Wakeford et al. 2017; Spake et al. 2018;

---

[19] NSF Graduate Research Fellow.

von Essen et al. 2018, 2020; Todorov et al. 2019). Because of its short (19.5 hr) orbital period, the hot Jupiter WASP-43b (Hellier et al. 2011) has been a prime target for phase-curve observations at infrared wavelengths with both the Hubble (HST; Stevenson et al. 2014) and Spitzer (Stevenson et al. 2017) Space Telescopes. These publications and related analyses (Kataria et al. 2015) invoked aerosols to explain the discrepancies between predictions and observations for exoplanetary phase-curve behavior (Stevenson et al. 2014, 2017; Kataria et al. 2015; Oreshenko et al. 2016; Haggard & Cowan 2018). Note that because the eclipse was detected in several IR observations, we can rule out the possibility that a nondetection (see below) in our HST WFC3/UVIS data, described here, would be caused by eccentricity modifying the eclipse time.

These phase-curve observations found little flux emanating from the nightside of the planet, suggesting thick cloud coverage. Furthermore, Keating & Cowan (2017) showed that reflected light eclipses can act as a pole arm for interpreting models from infrared observations, such as with the existing (i.e., HST and Spitzer) and future James Webb Space Telescope (JWST) observations.

Kataria et al. (2015) explored the potential for cloud formation to influence the phase-curve observations of hot Jupiter planets like WASP-43b and found that clouds could be a significant source of contamination in these observations. In canonical exoplanet cloud formation theory, using thermochemical equilibrium, planets with $T_{\rm eq} < 1650$ K are predicted to form substantial cloud layers of silicate materials, such as enstatite ($MgSiO_3$) or forsterite (Mg_2SiO_4; Ackerman & Marley 2001; Marley et al. 2013). The optical reflectivity of these silicates can be large enough that, under the most ideal conditions, observational simulations have shown that they could produce a geometric albedo >0.5. Furthermore, a geometric albedo of 0.5 for this hot Jupiter would produce NUV–optical eclipse depths of upward of 500 ppm (Oreshenko et al. 2016; Parmentier et al. 2016). In contrast, the majority of hot Jupiter models agree that albedos will be very low without clouds, providing an implicit metric for a priori cloud existence.

Here we present the first optical-to-NUV eclipse observations of WASP-43b. These observations leverage a mode on HST that has not previously been used in the study of exoplanet eclipse observations. We selected HST for this study because of its photometric ($\mathrm{rms}_{\rm reduced} = 172$ ppm) and pointing ($\Delta X \sim \Delta Y < 0.05$ pixels) stability, as well as the capacity for our achieved eclipse depth precision ($\delta_{\rm eclipse\ depth} \sim 34$ ppm).

In Section 2, we present the operations of HST's scanning mode observations including our newly developed `Arctor` pipeline for trace photometry (i.e., scanning mode arcs or asteroid streaks; see Appendix A as well). We present our results in Section 3, including comparisons to other known high-precision, reflected light eclipse depth measurements. Section 4 discusses our modeling campaign to consider how our upper limit provides context to cloud particle formation models. In Section 5, we continue with a discussion about how to use further reflected light observations of hot Jupiters to constrain cloud formation physics (Oreshenko et al. 2016). Finally, in Section 6, we present our conclusions.

2. Observations

We photometrically observed the hot Jupiter system WASP-43 during an eclipse event of the planet, which encompassed four HST orbits (see Figure 1).[20] This included an initial orbit to mitigate HST's postslew positional settling. The HST observed WASP-43b on 2019 July 3 from 00:14:59 UT to 05:40:02 UT, with our data being processed by the HST Data Processing Software System version HSTDP 2019.3. Below, we describe the choices, constraints, and capabilities of HST WFC3/UVIS for observing exoplanets with scanning mode visible light photometry.

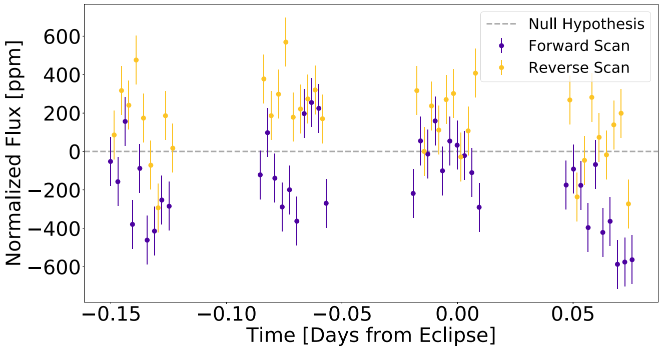

Figure 1. The HST WFC3/UVIS raw normalized flux light curve with forward scan values in violet and reverse scan values in orange. There is an apparent difference between the flux measured for forward and reverse scanned traces of 344 ppm.

Our program was one of the first transiting exoplanet programs to use HST WFC3/UVIS in photometric scanning mode. Lewis et al. (2020) and Wakeford et al. (2020) recently published spectral–temporal observations of the transiting exoplanet HAT-P-41b using the HST WFC3/UVIS. They achieved a 29–33 ppm precision over the G280 grism spectrum from 200 to 800 nm. Furthermore, Kenworthy et al. (2021; PI: Wang; HST 14621 and HST 15119) observed Beta Pic with HST WFC3/UVIS scanning mode observations to detect the predicted transit of the hill sphere for Beta Pic b and achieved a 57 ppm precision photometry from a narrow UV filter. Here we carefully describe our observational program and data analysis procedures to guide further programs and provide greater understanding of our considerations (see Appendix A for more details).

Because WASP-43, the host star, is moderately bright ($V_{\rm mag} = 12.4$) in our chosen filter (F350LP filter; 346–822 nm), we observed it using the HST WFC3/UVIS spatial scan mode with a scan rate of $0\farcs2278$ s^{-1}; the maximum scanning rate is $1''$ s^{-1}, limited by flight software. The HST placed the scan trace perpendicular to the read direction and located 179 pixel rows above the readout edge of the detector (see Figure 2). Each exposure lasted for exactly 82 s and spanned $18\farcs68$, or 467 pixels. The expected length of the trace required the use of a custom 400 × 951 WFC3 subarray aperture (see Figure 2) to maximize the signal-to-noise ratio (S/N) and ability to estimate the background while minimizing readout time.

This configuration provided 18–20 frames per orbit (10 forward scan and 10 reverse scan), culminating in 75 frames for the entire observation, including the initial orbit that established the precision of our pointing over the eclipse duration. This configuration resulted in a maximum pixel value of 48,000 e^-, with an estimated (median) background noise of 15 e^- per image.

---

[20] The complete data set can be retrieved from MAST: doi:10.17909/t9-47y9-v476.

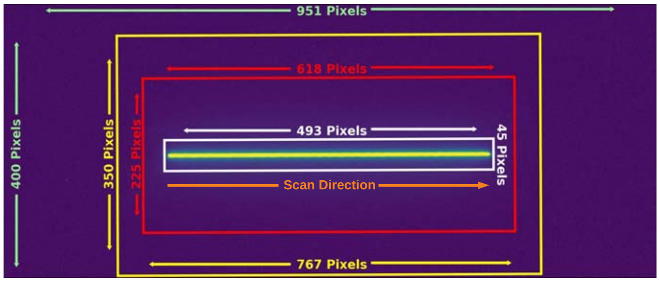

Figure 2. An HST WFC3/UVIS scanning mode observation example with apertures for photometry and background measurements. All pixels within the white rectangle are summed to measure the flux. The background region consists of the annulus region within the red and magenta rectangles. The values given represent the "best" photometry+model pair from our AICc and BIC analysis, with a 766 pixel aperture width × 45 aperture height for our photometry. The figure shows a larger photometry aperture (white) than the "best" solution pair.

We used the F350LP filter to maximize throughput and spectral coverage without saturating the detector. Comparing the photon noise predictions from the official HST WFC3/UVIS, etc.—with multiple filter/scanning rate/integration time combinations—our configuration provided the minimum predicted uncertainty per image and maximum number of frames per eclipse. These observations resulted in a photometric uncertainty on the integrated flux per image of 124 ppm (S/N ∼ 8065) and a global scatter over the raw light curve (i.e., rms) of 206 ppm.

2.1. Data Reduction

We developed a novel `Python` package that is optimized for extracting photometric HST WFC3/UVIS scanning mode time-series observations; this is the first UVIS photometric scanning package to be released open source as a reusable package. We named it `Arctor` because it is optimized to extract photometry from arcs on images, i.e., traces. Our software may also be relevant to surveys observing near-Earth objects that streak across their detectors. The package is publicly available and BSD-3 licensed on our `GitHub` page.[21]

`Arctor` performs standard astronomical photometric extraction, but it is adapted for scanning mode observations, which spread the light across the detector to maximize the instrument's duty cycle. The special considerations for scanning mode include using rectangular apertures for flux, median, and column-wise background estimation, as well as several other detailed considerations discussed in Appendix A.

After downloading the entire data set from MAST (`mast.stsci.edu`), we also extracted the necessary planetary parameters from `exo.mast.stsci.edu`[22] (Mullally et al. 2019). For our analysis, we only needed to examine the 75 flat-field corrected (FLT) fits files.

`Arctor` examined the positional coordinates (POSTARGs) to identify which observations are associated with forward and reverse scanning directions. We used the time stamps to identify and map temporal correlations with the correlated noise and astrophysical signals.

Our primary operations were to extract the photometry and scanning trace properties, i.e., y-positions (cross-scan spatial pixel position), x-positions (read direction spatial pixel position), trace angles (relative to mid-trace), and trace lengths, as well as the frame indices corresponding to the forward and reverse scanned observations. Moreover, we also computed the sky background with both static and scanning-focused methods; we then computed the cosmic-ray mask along the temporal axis (i.e., statistical outlier rejection in time per pixel).

2.2. Data Analysis

After extracting the photometric time series, we used four independent model selection methods (i.e., corrected Akaike information criterion, AICc, and Bayesian information criterion, BIC) to diagnose whether any of the features listed above were correlated with the flux (see Figure 3). We used `Arctor` to fit both maximum a posteriori (MAP) solutions and Markov Chain Monte Carlo (MCMC). We explored the posterior probability distribution using a Hamiltonian Monte Carlo (HMC[23,24]; Salvatier et al. 2016; Foreman-Mackey et al. 2020). By including our photometric uncertainties (∼124 pmm), we generated our eclipse depth (and other parameters') uncertainties from the Bayesian credible regions (BCRs) derived by our MCMC posteriors (see Figure 3).

The HMC package (`exoplanet`) that we used includes a variant of both BATMAN and `STARRY` to model transiting exoplanet observations (Kreidberg 2015; Luger et al. 2019; Foreman-Mackey et al. 2020). This provided a fully analytic transit light curve, including ingress, egress, and limb darkening (Mandel & Agol 2002). Because the `exoplanet` package was built for transit modeling, we required the eclipse depth to be positive. To establish proper Bayesian posterior bounds, we tested multiple priors—uniform, lognormal, log-uniform—all of which resulted in a nondetection with similar uncertainties over the eclipse depth. Moreover, we sampled 16 HMC chains for the 25 light curves that sustained the 25 lowest AIC/BIC from the MAP analysis, discussed above. Each of our light curves included the eclipse light-curve model (Mandel & Agol 2002) and a combination of linear systematic trends with respect to time, x-position, y-position, trace length, and trace angle. We did not explore nonlinear systematic trends, but we tested the validity of our final result by including Gaussian processes (GPs; Gibson et al. 2012a, 2012b; Foreman-Mackey et al. 2020) and computing the AIC/BIC with it as well (see below). The convergence of each set of 16 chains was confirmed through both inspection of the autocorrelation figure and the Gelman–Rubin test, provided by the `exoplanet` package.

After deriving our best model, we further diagnosed the existence of residual autocorrelated noise sources (i.e., power-law noise). We diagnosed several techniques: Carter & Winn (2009) wavelets, residual binning technique (Pont et al. 2006; Cubillos et al. 2017), and GPs (Foreman-Mackey et al. 2017). Our MCMC analysis with GPs did not recover the existence of significant autocorrelated noise; see Appendix B.2 for further details.

Assuming that no eclipse occurred during our observations, and not accounting for any systematic noise sources—i.e., if only Gaussian noise existed—then we estimated that the minimum eclipse depth that our data could have detected at 3σ would be 102 ppm (i.e., $\sigma = \frac{206}{\sqrt{75}} \times \sqrt{2} \sim 34$ ppm and thus

---

[21] github.com/exowanderer/arctor; a branch concurrent with this article can be found at https://github.com/exowanderer/arctor/tree/apj_publication_static_version_30.06.2020.

[22] `exoMAST-API`: github.com/exowanderer/exomast_api.

[23] PyMC3: https://github.com/pymc-devs/pymc3.

[24] Exoplanet: https://github.com/dfm/exoplanet.

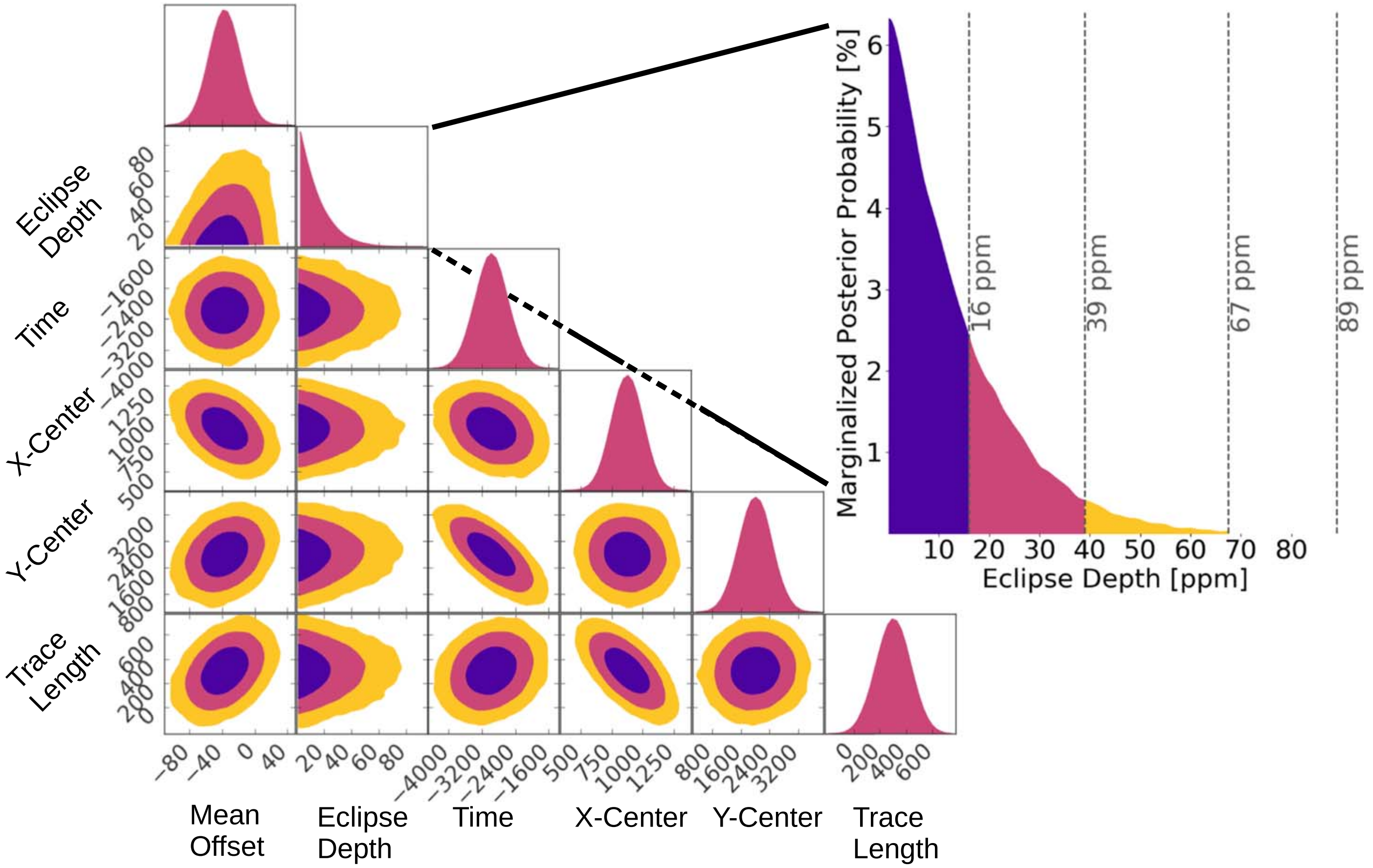

Figure 3. Corner plot with eclipse kernel density estimates. The corner plot is a sequential 2D correlation and marginalization description of the MCMC chains. The kernel density estimate inclusion (upper right) shows a smoothed representation of the histogram over the MCMC posterior for the eclipse depth alone. All five non-eclipse depth measurements are properly bounded as Gaussian posteriors (see diagonals). The asymmetric behavior of the eclipse depth posterior is representative of our nondetection. Using quintile analysis, we derived that 3σ (99.7%) of the chains were sampled within 67 ppm, which sets our upper limit used throughout this paper.

$3\sigma \sim 102$ ppm). Our final 3σ upper limit, after modeling the correlated noise sources, achieved $3\sigma \sim 67$ ppm—a >34% reduction in global noise sources, which reveals the effect of inflated uncertainties from non-modeled correlated noise.

We provide a detailed description of `Arctor`, our novel pipeline for photometry scanning mode observations, in Appendix A. Furthermore, in Appendix B, we show the results from our 12,800 MAP fits to derive the AICc and BIC values to select the most viable set of features and hyperparameters for optimizing the information extraction from our observations (AICc and BIC are defined in Appendix B). We used our 12,800 MAP fits to probe the span of all possible combinations of our hyperparameters: linear trends (time, x-position, y-position, trace length, trace angle), aperture width, and aperture height for our rectangular apertures.

3. Results

The overarching result from our observations is that the dayside of WASP-43b is very dark. Integrated over the entire optical band (346–822 nm), we derived an upper limit to the reflected light eclipse depth of less than 67 ppm, corresponding to a geometric albedo of $A_g \lesssim 0.06$ (3σ upper limit); see Figures 3–5.

Our individual frames sustained an average 124 ppm photometric uncertainty, which was a <1% difference from the predicted photon+read noise using the HST WFC3/UVIS, etc. This resulted in our best AICc parameter set generating a light curve with the standard deviation of the normalized residuals (SDNR) = 172 ppm and a model uncertainty on the eclipse depth of 34 ppm.

Figure 4 shows the best-fit eclipse depth (9 ± 34 ppm), along with other predictive eclipse depths for relevant cloud models (see below). Our lack of detection of an optical eclipse depth implies a lack of reflective clouds on the dayside within the layers probed by eclipse observations ($P \lesssim 1$ bar).

Our derived upper limit of 67 ppm corresponds to a geometric albedo, $A_g \lesssim 0.06$. Kepler (and subsequently K2) detected the optical eclipse of more than a dozen hot Jupiters (Esteves et al. 2015). Figure 5 displays their geometric albedos as a function of equilibrium temperatures ($T_{\rm eq}$), which includes several detected reflected light eclipses in a similar wavelength range (~600 nm) to our HST WFC3/UVIS F350LP observations. Compared to this set of Kepler reflected light results, our nondetection would imply that the atmosphere is less likely to sustain clouds (in the observational regime) than planets with similar $T_{\rm eq}$, i.e., within ~100 K of WASP-43b (Esteves et al. 2015; Niraula et al. 2018).

Figure 5 places our reflected light geometric albedo upper limit within the context of many known high-precision measurements with $1000\,{\rm K} < T_{\rm eq} < 2000\,{\rm K}$, all from space-based facilities. Our observation is not the highest-precision

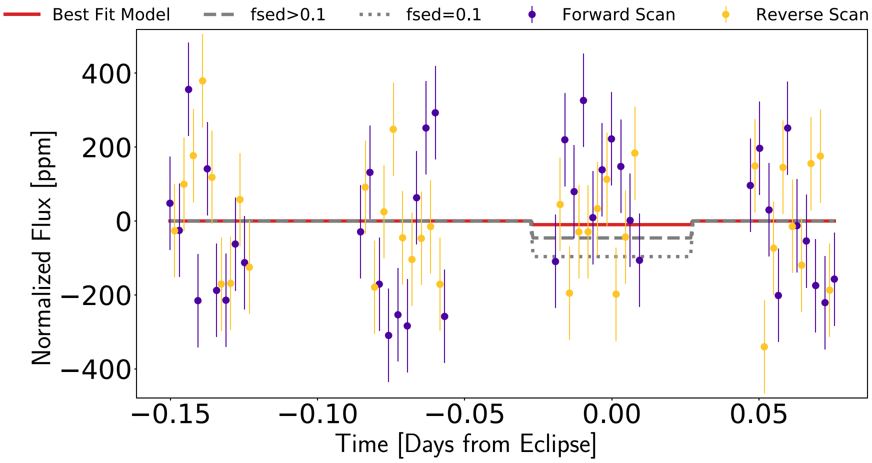

Figure 4. The HST WFC3/UVIS normalized flux light curve with forward scan values in violet and reverse scan values in orange. The error bar points are corrected from fitted systematic behavior involving linear trends with respect to *x*-centers, *y*-centers, and trace lengths. The pale violet and orange background points represent the raw flux values from our rectangular photometric extraction. The models shown here represent our best AICc- and BIC-derived model (red solid line), our predicted eclipse model with $f_{\rm sed} = 0.1$ (gray dotted line), and our predicted eclipse model with $f_{\rm sed} > 0.1$ (gray dashed line). The $f_{\rm sed} = 0.1$ model is not consistent with our observational results, while $f_{\rm sed} > 0.1$ is consistent with our 3σ upper limit.

(The data used to create this figure are available.)

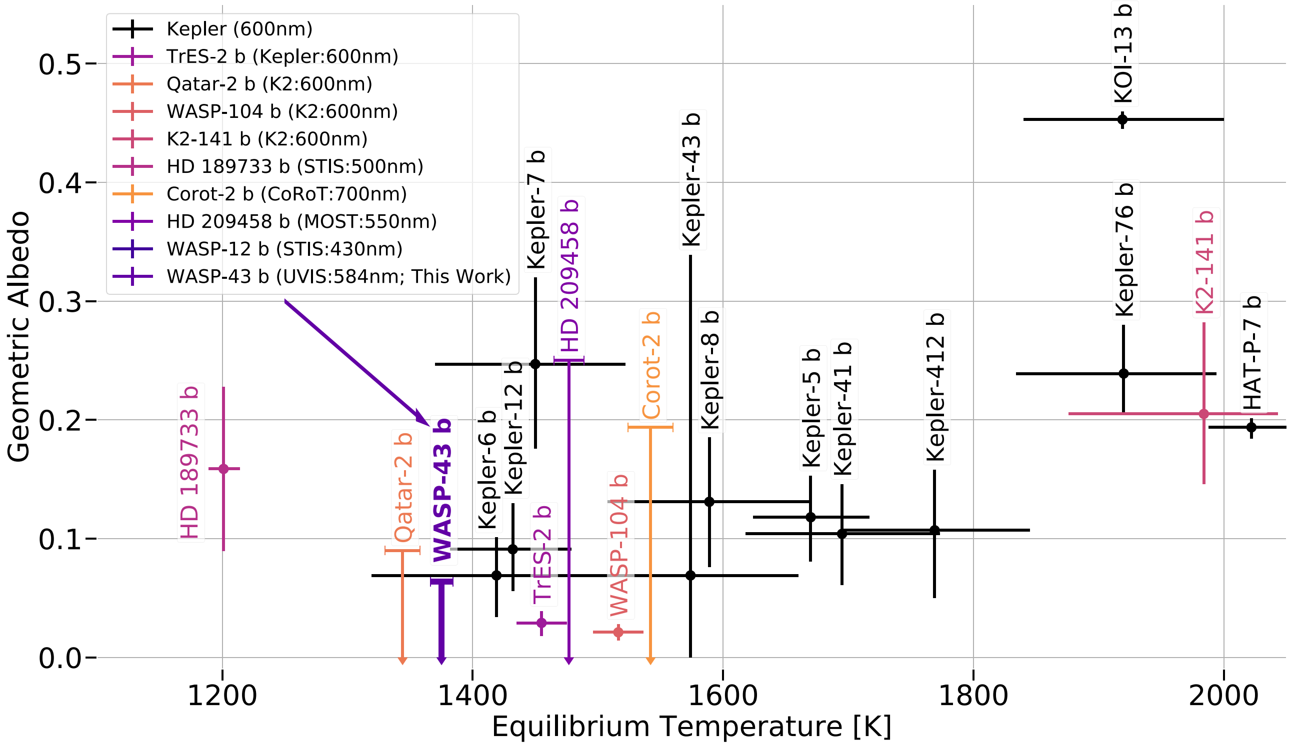

Figure 5. Apparent geometric albedo comparisons from similar observations of reflected light eclipses from hot Jupiters. All upper limits are reported here as 3σ upper limits. The black dots represent results from the Kepler mission (Angerhausen et al. 2015; Esteves et al. 2015; Shporer & Hu 2015; Bell et al. 2017). The Kepler points were observed at 600 nm, which sustains substantial contamination from atomic absorption contamination and (likely) thermal emission. The HD 189733b reflected light observations were observed with HST/STIS, which sustained $\sim 2\times$ our uncertainties (Evans et al. 2013; Bell et al. 2017). Our WASP-43b HST WFC3/UVIS observations sustained the most precise upper limit attained in this wavelength and (equilibrium) temperature range.

geometric albedo constraint, but it is equivalent to observations with multiple epochs, i.e., TrES-2b and WASP-104b, both observed with K2. In contrast, it is the most precise geometric albedo upper limit and at the second-lowest $T_{\rm eq}$.

The distribution of geometric albedos over equilibrium temperatures shown in Figure 5 reveals an apparent linear trend, such that hotter planets have a larger geometric albedo. On the other hand, given the limited data, large uncertainties, and possible thermal contamination for the hottest planets, this trend is not conclusive.

Comparing to the thermal infrared phase-curve results (see Figure 6), WASP-43b does appear to have an anomalously large thermal day-to-night contrast (Stevenson et al. 2017), implying a lack of significant atmospheric circulation; combined with the apparent lack of observable clouds on the dayside of the planet, this could imply that the thermal phase-

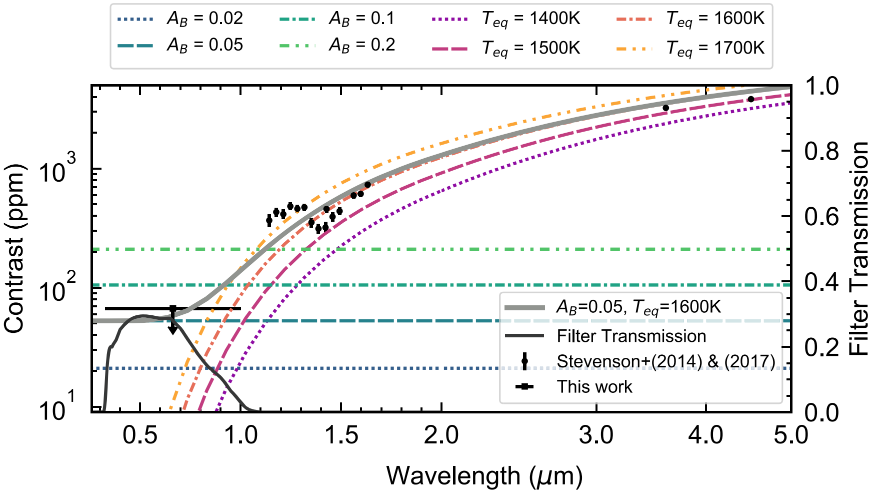

Figure 6. Toy model example of what Bond albedos and equilibrium temperatures are allowed by the HST observations presented here, the HST WFC3 data of Stevenson et al. (2014), and the Spitzer data of Stevenson et al. (2017). With horizontal lines, we show $A_B = 0.02$, 0.05, 0.1, and 0.2, along with several blackbodies in shades of purple to orange of $T_{\rm eq} = 1400$, 1500, 1600, and 1700 K. The example combination of $A_B = 0.05$, $T_{\rm eq} = 1600$ K allowed by the data is shown in gray, implying that the planet is very dark on the dayside.

Table 1
Planetary and Stellar Parameters Assumed in Atmospheric Modeling

Parameter	Value
P	0.81347 days
a	0.01526 au
i	82°33
$M_{\rm p}$	2.05 $M_{\rm J}$
$R_{\rm p}$	1.036 $R_{\rm J}$
g	47.342 m s^{-2}
M_*	0.717 M$_\odot$
R_*	0.667 $R_\odot$
$T_{\rm eff}$	4300.0 K

curve observations are the result of different pressure levels being observed at the dayside, as compared to the limbs and nightside of the planet (i.e., maintaining $\tau \sim 1$; Stevenson et al. 2014, 2017; Kataria et al. 2015).

4. Modeling

The eclipse depth indicates that the reflected light and/or thermal emission from the planet is very low over this NUV/optical bandpass. The predicted dayside temperature of the planet ranges between 1400 and 1600 K at observable wavelengths (Kataria et al. 2015; Stevenson et al. 2017). Thus, in order to produce a suitably low eclipse depth, we can predict a maximum allowable albedo in the optical photometric band. Figure 6 shows a toy model schematic of potential possibilities. The model combines the reflected light signal expected from a planet with a monochromatic Bond albedo (the fraction of the total light reflected compared to incident stellar light) of 0.02, 0.05, 0.1, or 0.2 with the thermal emission expected from a blackbody of 1400, 1500, 1600, or 1700 K. Given the eclipse depth upper limit of 67 ppm, the planet must be very dark, and we can expect it to have a Bond albedo of 0.06 or less on its dayside hemisphere.

Previous studies of WASP-43b predict Bond albedos of $0.36^{+0.11}_{-0.12}$ (Schwartz & Cowan 2015) and 0.3 ± 0.1 (Keating & Cowan 2017) using day and night temperature differences or geometric albedo conversions, which are ultimately an assumption about the bolometric flux from around the planet, such as the technique used by Stevenson et al. (2017) to measure $0.19^{+0.08}_{-0.09}$. Each technique is limited by our ability to assume the correct spectral energy distribution (SED) of the planet, as well as the stellar SED. General circulation models (GCMs) can provide a framework to explore the planet holistically.

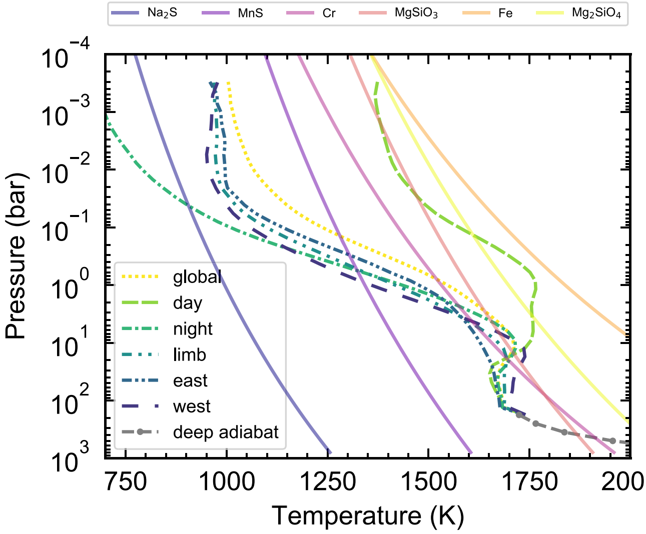

Figure 7. Temperature–pressure profiles from Kataria et al. (2014) along with the condensation curves of several cloud species (Morley et al. 2012). If the convective region deep in the atmosphere is hotter, Cr and the Mg species will likely only condense in the deep interior. Thus, we expect Na_2S and MnS to be the only species available at the pressure probed by our observations.

We explored the possible atmospheric scenarios using pressure–temperature files and the associated vertical mixing profiles (K_{zz}) generated in the GCMs from Kataria et al. (2014), which assume a cloudless atmosphere in chemical equilibrium. To compare our results with published WASP-43b atmospheric models (i.e., Kataria et al. 2015), we used the same planetary and stellar parameters of Hellier et al. (2011), which can be found in Table 1. The temperature–pressure profiles are shown in Figure 7, overplotted on condensation curves for several

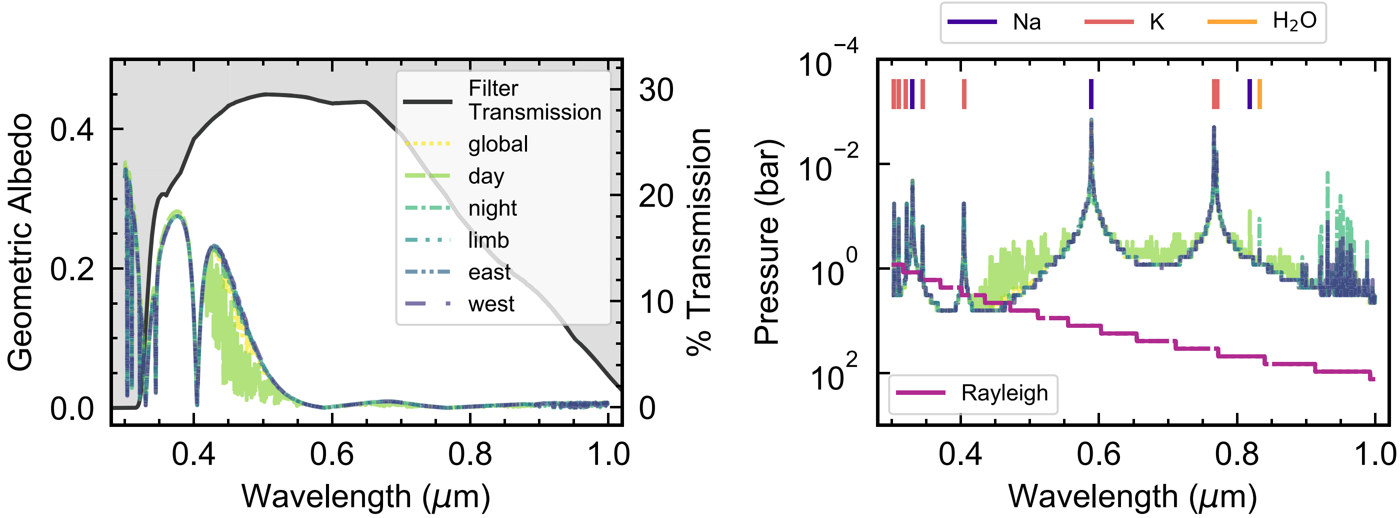

Figure 8. Geometric albedos for the cloudless cases. Left: geometric albedo for each of the six profiles. Right: photon attenuation diagram. The lines correspond to the pressure level at which the two-way optical depth in the atmosphere reaches $\tau = 0.5$, caused by the gas absorption (colors and line styles corresponding to the left panel) and cloud or Rayleigh scattering. Without clouds, the gas chemistry variations between the GCM averages produce the observed albedo spectrum variations. The lines are slightly transparent to demonstrate how similar the gas chemistry is among all other profiles. We mark the positions of prominent Na, K, and H_2O (on the nightside model only) absorption lines. The less prominent lines near 0.5, 0.7, and 0.9 μm are due to TiO and VO in the dayside model. The nightside instead shows H_2O and CH_4 lines beyond 0.9 μm.

cloud species. Starting from the deep interior, as the planet's upper layers decrease in temperature, a particular cloud species may condense with a cloud base at the intersection of the condensation curve and the temperature–pressure profile.

We used the cloud code developed by Ackerman & Marley (2001) to compute cloud profiles derived from temperature–pressure profiles from Kataria et al. (2014). We allow Na_2S, MnS, Cr, and $MgSiO_3$ to condense. We also test five sedimentation efficiencies, $f_{\rm sed}$, which control the particle size and vertical extent of the cloud. A smaller $f_{\rm sed}$ yields clouds that are vertically extensive, while larger $f_{\rm sed}$ values yield vertically thin clouds. We then used `PICASO` (Batalha et al. 2019) to generate the geometric albedo spectrum of each case (36 cases), i.e., when the full-phase dayside appears at secondary eclipse. Note that the geometric albedo spectrum is defined to be at full phase. The nightside average spectrum would never be observed in such a geometry but is illustrative to show the variations in cloud structure inferred around the planet. We used the opacity database supplied with the initial public release and a PHOENIX model representation of WASP-43 (STScI Development Team 2013; Batalha 2019).

The geometric albedos for the cloudless cases are shown in the left panel of Figure 8 and can be understood by examining the photon attenuation diagram in the right panel. The lines correspond to the pressure level at which the two-way optical depth in the atmosphere reaches $\tau = 0.5$, caused by the gas absorption and cloud or Rayleigh scattering. Without clouds, albedo differences are driven by the gas chemistry with the largest features being caused by Na and K, as well as water at longer wavelengths. The hotter dayside (dotted lines) shows additional gas opacity lines (such as near 0.5 μm), which are caused by TiO and VO; this is reflected in a much darker albedo spectrum in those wavelength regions but is a weak effect.

Once clouds are added, the location of the cloud varies across the planet, and how high the cloud particles are lofted begins to affect the albedo spectrum. In Figure 9, we show the results of the cloudy cases where Na_2S, MnS, Cr, and $MgSiO_3$ are allowed to condense at depth. From top to bottom are the different sedimentation efficiency cases for global average, dayside, nightside, limb average, and east or west limb (the temperature–pressure profiles are shown in the right panel). In nearly all profile scenarios, the $f_{\rm sed} = 3.0$ cloud scenario is very similar to the cloudless case presented in Figure 8. The shape is then modulated by continuing to loft the clouds higher and higher into the atmosphere such that the cloud begins to dominate over Rayleigh scattering and gas absorption, leading to a darker albedo spectrum at short wavelengths, but also increases the reflectivity at long wavelengths.

In agreement with the previous conclusions of Kataria et al. (2015), we predict that the nightside should readily produce clouds (the uppermost is Na_2S). These clouds should be high enough in the atmosphere that, at various sedimentation efficiencies, they make a significant impact on the albedo spectrum; the effect is to darken the spectrum at shorter wavelengths and brighten it at longer wavelengths. For smaller particles, Na_2S gets darker beyond 1 μm, but for larger particles, it predominantly remains at the same brightness. The pressure at which the cloud(s) exist will determine the observed brightness temperature and albedo. Therefore, the observed brightness temperature can constrain their sedimentation efficiency and related particle sizes. The most significant effect is that a $MgSiO_3$ cloud layer would serve to dramatically brighten the albedo spectrum.

On the dayside, spectroscopy may be capable of determining the presence of TiO and VO in the gas phase by determining the albedo near 0.5 μm. The model is unable to condense a cloud at observable pressures on the dayside unless $MgSiO_3$ is included, and even then, only for the smallest $f_{\rm sed}$. In the smallest sedimentation efficiency case, some small particles are mixed up through the atmospheric temperature inversion in the dayside profiles, thereby delivering condensable gas to higher regions of the atmosphere where it can once again condense. Note that WASP-43b has an exceptionally high gravity ($g \sim 51$ m s^{-2}) compared with other hot Jupiters like Kepler-7b ($g \sim 4$ m s^{-2}).

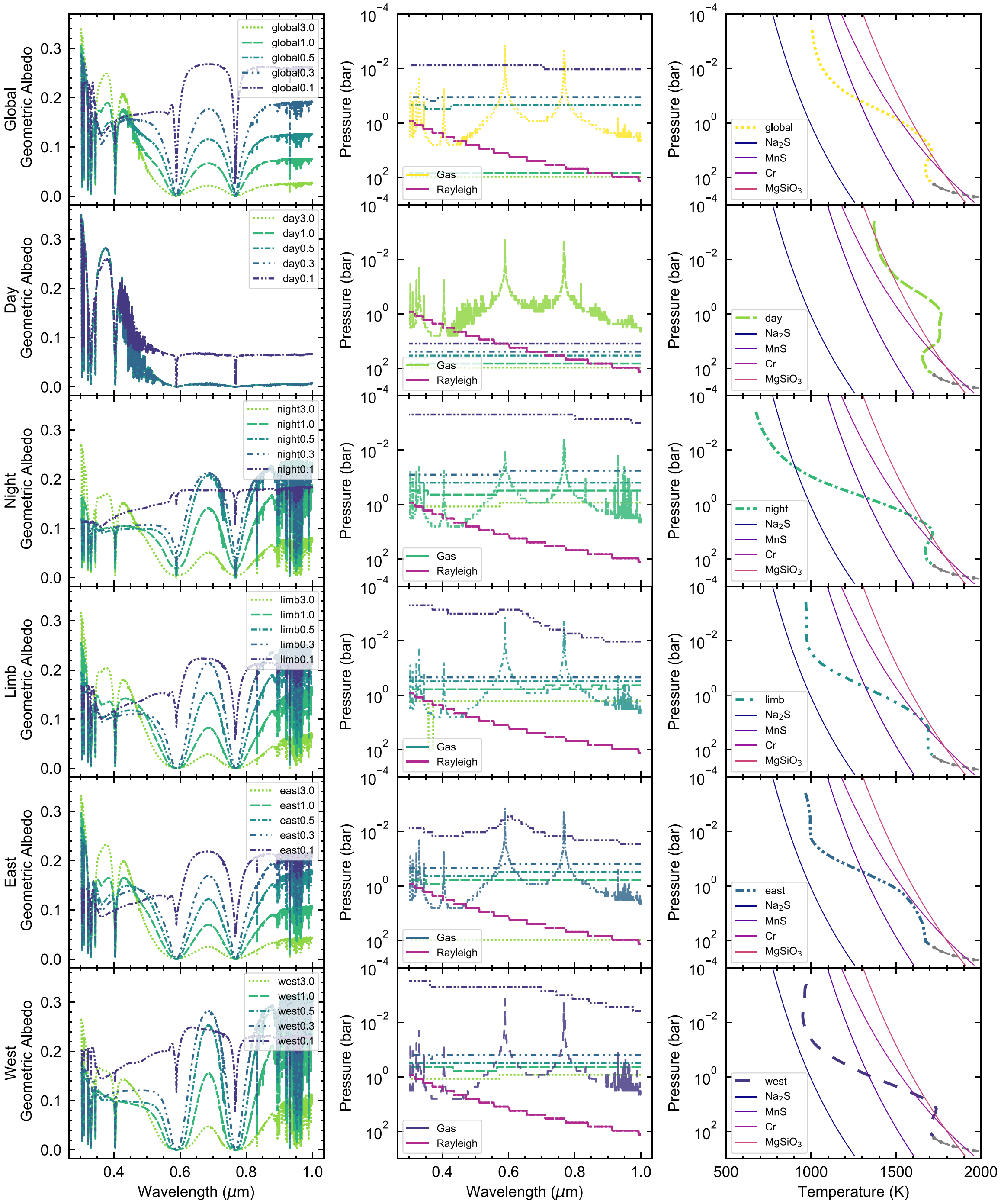

Figure 9. Geometric albedos for the cloudy cases. Each row is a different profile from Kataria et al. (2015). Left: geometric albedo spectrum for each of the five sedimentation efficiencies. Middle: photon attenuation diagram showing the pressure level at which the two-way optical depth in the atmosphere reaches $\tau = 0.5$, caused by the gas absorption and cloud or Rayleigh scattering. Line styles and colors for the cloud opacity correspond to their geometric albedo spectrum counterparts. Note the pressure level where clouds contribute changes with $f_{\rm sed}$. Right: temperature–pressure profile overlaid on the cloud condensation curves. All profiles readily produce clouds, of which only the most lofted begin to dominate as an opacity source, except for the dayside profile.

As a result, in the absence of particles representing a small $f_{\rm sed}$, the albedo spectrum would be dark, which is consistent with the upper limit derived from the data; this would imply that it is entirely dominated by gas absorption. More aggressive vertical mixing schemes are able to deliver more $MgSiO_3$ particles to observable pressure, but the particles grow in size, which makes them less reflective. Whether or not such a second cloud layer would form in a realistic atmosphere, as opposed to the idealized case studied here, would take more sophisticated modeling.

The models and data continue to suggest that WASP-43b has inhomogeneous cloud coverage, where the dayside has essentially no observable clouds, while the limbs and nightsides are able to condense all four cloud species. Typically, the uppermost cloud is MnS, except on the nightside, where the models predict Na_2S to be the uppermost cloud. In contrast, if the bright $MgSiO_3$ particles are comparatively smaller, they become more difficult to sequester with depth. The subsequent cloud layer would extend to the top of the atmosphere and

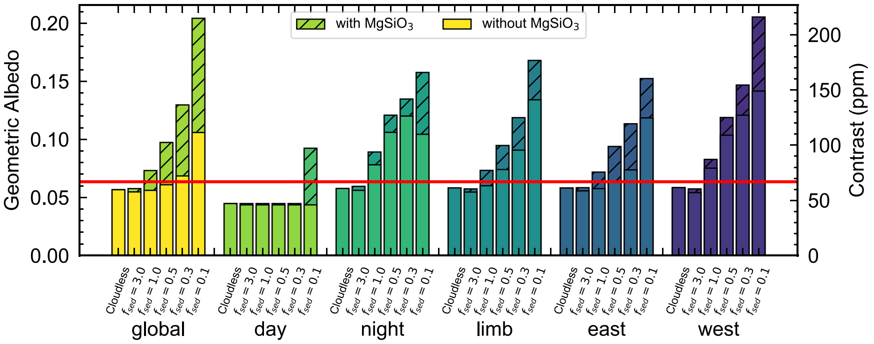

Figure 10. Filter-integrated geometric albedos of all model cases excluding (solid bars) and including (hatched bars) $MgSiO_3$ condensates. Our measured constraint on the observational 3σ limit (in contrast) is represented by the horizontal red line. Our upper limits imply that the $f_{sed} = 0.1$ dayside model is not consistent with our data; we infer from this that either small lofty particles are not being propagated into the upper atmosphere (i.e., the observable regime; $P \lesssim 1$ bar) or cloud-forming particles are sequestered in the deep reaches of the planetary atmosphere. Connecting this to the condensation curves in Figure 7, we can infer that $MgSiO_3$—which thermochemical equilibrium would predict to form clouds at $P \lesssim 1$ bar—may have formed clouds within the deep adiabat, thus significantly reducing the available mass to form clouds near our observational regime.

become the dominant source of cloud opacity at all planetary longitudes.

From each model, we filter-integrate the albedo spectra and compute the expected flux contrast. `PICASO` is also able to compute the thermal emission shortward of 1 μm, and the expected thermal contamination is negligible. These contrasts are shown in Figure 10. The dayside is consistent with a null detection of a secondary eclipse. The data rule out the presence of highly lofted $MgSiO_3$ clouds. If it did condense in the dayside atmosphere, only the most lofted scenario (forming a second cloud deck near 10 mbars) would have been detectable. Our models suggest that the pressures being probed by nightside and dayside observations are drastically different because the clouds are more significantly lofted on the nightside relative to the dayside.

5. Discussion

Our modeling results (described in Section 4) revealed that to sustain this nondetected reflected light eclipse, the dayside atmosphere must significantly lack particles lofted into the observable part of the atmosphere. The models suggest that only the most lofted cloud case scenario, $f_{sed} = 0.1$, could escape a cold trap at the deepest layers of the atmosphere to condense into a second upper cloud layer, which could lead to a detectable optical eclipse depth. All of the rest of our modeled sedimentation efficiencies led to particles being trapped at deeper pressures; they were thus unable to be mixed upward and recondensed. The fact that we did not detect an optical eclipse confirms that we can rule out a high-altitude, bright, uniform cloud layer.

At planetary longitudes away from the substellar point, the upper atmosphere of the planet is predicted to be cool enough to condense other species, notably, Cr, which is also potentially sequestered deep in the atmosphere; MnS; and, on the nightside, perhaps even Na_2S. If the cloud behavior can be parameterized with $f_{sed} < 0.5$, then these species may lead to an observable phase-curve signature, especially at optical wavelengths. The f_{sed} values less than 1 have been increasingly necessary to describe the observations of hot Jupiters such as Kepler-7b (Demory et al. 2013; Webber et al. 2015). If $MgSiO_3$ is not sequestered at depth, or simply not lofted high enough into the upper atmosphere, then the planet would be brighter at other observed phase angles where the temperatures are cooler, allowing larger particles to be more easily lofted to form clouds at observable pressure ranges (see again Figure 10). If silicate clouds are trapped in the deep convective layers of the atmosphere, then our observations would be unlikely to observe them at lower pressures (Powell et al. 2018). On the other hand, Cr has a deeper cloud base in the dayside profile; this could thus require more vigorous vertical mixing, with even smaller particles, to reach the upper altitudes where our observations might be able to detect their reflected light.

Determining the parameters for clouds in the atmosphere of WASP-43b may constrain whether this planet follows in the footsteps of its brown dwarf cousins or, instead, low-gravity hot Jupiters. The presence of partially cloudy (i.e., patchy) daysides for planets spanning a wide range of equilibrium temperature led Parmentier et al. (2016) to conclude that the cloud composition must vary with the equilibrium temperature of the planet. This would imply a transition in cloud composition similar to the L/T transition in brown dwarf atmospheres. With an equilibrium temperature of 1450 K, WASP-43b is close to this proposed boundary for such a planetary L/T transition but with a higher gravity than many of its peers. The precise equilibrium temperature at which the trapping mechanism can become effective depends on the species in question and the deep thermal structure of the planet, which is unconstrained by existing observations (Thorngren et al. 2019).

Because of its observational and atmospheric viability for spectroscopic detections, WASP-43b has become a benchmark planet for current and future hot Jupiter observations. Upcoming observations by JWST for both ERS (PI: Batalha) and GTO (PI: Birkmann) include ~48 hr of JWST observations to map the thermal structure and chemical composition of this exoplanet with exquisite detail (Bean et al. 2018; Venot et al. 2020). We expect that no other exoplanet has been or will be observed with this much precision and wavelength coverage for many years to come. And yet, all of these observations probed or will probe the atmosphere at >1 μm; in contrast, optical light (<1 μm) is the primary component of the atmospheric energy budget that is a direct probe of cloud distributions, particle size, and composition.

Our lack of understanding about cloud properties—effective height composition, patchiness at the limb, particle size—is currently a significant limitation to measure precise molecular abundances in hot Jupiter atmospheres (Ormel & Min 2019). With WASP-43b, Kataria et al. (2015) hypothesized that inhomogeneous clouds could explain the lack of nightside flux from WASP-43b, as observed in both HST WFC3/IR and Spitzer phase curves (Stevenson et al. 2014, 2017). The presence of such inhomogeneous clouds would increase the longitudinal brightness contrast of its atmosphere—cloudy at the limb, clear near the substellar point. The extent, composition, and distribution of aerosols in exoplanet atmospheres is one of the most significant standing questions in exoplanet characterization research. Not accounting for inhomogeneous clouds could lead to biases in atmospheric abundance retrievals and even more spurious molecular detections when the exoplanetary spectrum is interpreted with independent 1D models at multiple phases, which is usually the case (Feng et al. 2016). Our WASP-43b optical eclipse measurement is conclusive that clouds are not uniform or bright, but to distinguish between several other implications of our result, we would need a full phase curve of WASP-43b at NUV or optical wavelengths.

6. Conclusions

We observed WASP-43b during secondary eclipse with four HST orbits using the HST WFC3/UVIS channel in scanning mode. Because this is one of the first transiting exoplanet programs to use HST WFC3/UVIS in photometric scanning mode, we described our observational program and data analysis procedure in detail (see Appendix A). We created a new, multifunctional code for arc photometry, called `Arctor`,[25] which can be used for high-precision photometry of all HST WFC3/UVIS scanning mode observations and may also be useful for near-Earth object streak observations. Using the F350LP filter, we did not detect an eclipse of WASP-43b during our observations. As a result, we robustly constrained an upper limit on the eclipse depth of 67 ppm with 3σ confidence. We determined this upper limit by integrating under the marginalized uncertainty distributions, as seen in Figure 3, up to 99.7% posterior probability.

This upper limit on the eclipse depth is consistent with a very low dayside geometric albedo (<0.06) for WASP-43b. Using a combination of 3D GCMs and cloud condensation models, we estimated the range of planet-to-star contrasts expected under various thermal and cloud sedimentation efficiency regimes. We find that our measured upper limit on the visible wavelength eclipse depth of WASP-43b is inconsistent with significant cloud coverage on the dayside of WASP-43b. This finding indicates that if clouds are forming in other regions of the planet's atmosphere, such as on the nightside or at higher pressures, they are not being efficiently transported into the portions of WASP-43b's dayside atmosphere probed by the observations presented here.

WASP-43b is one of the best-studied exoplanets to date, with multiwavelength transmission, emission, and now reflected light observations spanning the visible to infrared. Its relatively high average gravity and short orbital period make it, thus far, a unique laboratory for testing how these planetary properties shape atmospheric physics. Further observations are needed to better understand the 3D thermochemical structure of this intriguing planet. There are currently planned phase-curve observations of WASP-43b by JWST with GTO 1224 (PI: Birkmann) and ERS 1366 (PI: Batalha; Bean et al. 2018; Venot et al. 2020). These future observations will probe the infrared emission of WASP-43b as a function of orbital phase from 2.5 to 12 μm. They are expected to provide an exquisite look into WASP-43b's atmosphere but may not provide a complete picture of processes like cloud formation. Our results and models show that further observations of WASP-43b at optical wavelengths, with narrower bandpasses or spectroscopy, and at multiple orbital phases are needed to better understand the processes shaping WASP-43b's low dayside geometric albedo.

This work is based on observations made with the NASA/European Space Agency Hubble Space Telescope that were obtained at the Space Telescope Science Institute (STScI), which is operated by the Association of Universities for Research in Astronomy, Inc., under NASA contract GO-15473. The authors thank Mark Marley for discussions that greatly improved the modeling efforts of this manuscript. Work performed by L.C.M. was supported by the Harvard Future Faculty Leaders Postdoctoral fellowship. This work could not have been completed without the fundamental opacity work by Richard Freedman and Roxana Lupu. The authors are grateful to Drs. Dan Foreman-Mackey and Eric Agol for detailed conversations about autocorrelated noise, Gaussian processes, and fundamental statistics. The research leading to these results received funding from the European Research Council (ERC) under the European Union's Horizon 2020 research and innovation program (grant agreement No. 679633; Exo-Atmos). This research has made use of the NASA Exoplanet Archive, which is operated by the California Institute of Technology, under contract with the National Aeronautics and Space Administration under the Exoplanet Exploration Program. This project made use of the exo.mast[26] web service (and API) hosted by the Mikulski Archive for Space Telescopes (MAST) at STScI (Mullally et al. 2019). STScI is operated by the Association of Universities for Research in Astronomy, Inc. This research was fostered by members of the Space Telescopes Advanced Research Group on the Atmospheres of Transiting Exoplanets (STARGATE) Collaboration.

Facilities: Hubble Space Telescope, MAST, NASA Exoplanet Archive.

Software: numpy (Harris et al. 2020), `Astropy` (Astropy Collaboration et al. 2013, 2018), `celerite` (Foreman-Mackey et al. 2017), scipy (Virtanen et al. 2020), matplotlib (Hunter 2007), pandas (Wes McKinney 2010), `Photutils` (Bradley et al. 2019), PICASO (Batalha et al. 2019), pymc3 (Salvatier et al. 2016), exoplanet (Foreman-Mackey et al. 2020), exomast_api (https://github.com/exowanderer/exomast_api), autograd (https://github.com/HIPS/autograd), theano (Theano Development Team 2016).

Appendix A
Arctor HST WFC3/UVIS Scanning Mode Photometry Pipeline Configuration

Here we describe our novel pipeline, `Arctor`, which is optimized to extract exoplanet transit and eclipse light curves from HST WFC3/UVIS photometric light curves in scanning mode. It may also be useful for near-Earth object flux estimates for streak observations. `Arctor` performs similar tasks to standard aperture photometry, except that it is optimized for scanned images, which leave a trace on the detector, instead of a PSF. `Arctor` is novel because it is the first photometric

---

[25] https://gihub.com/exowanderer/Arctor

[26] exo.mast.stsci.edu

scanning mode pipeline to be released for open-source development and use, and it implements several key algorithms that are not necessary for nonscanning mode observations and new Bayesian inference techniques that have not been included in other transiting exoplanet pipelines.

After downloading the entire data set from `mast.stsci.edu`, we also extracted the necessary planetary parameters from `exo.mast.stsci.edu`[27] (Mullally et al. 2019). We examined the 75 provided FLT files (FLT represents that the files have been calibrated and flat-fielded using HST's CALWF3 pipeline). `Arctor` examines the header files from the FLT files to extract the following.

1. `EXPEND` and `EXPSTART` to estimate the observational time as $\mathtt{time}_k = \frac{1}{2}(\mathtt{EXPSTART}_k + \mathtt{EXPEND}_k)$.
2. `POSTARG1` and `POSTARG2`, which represent the spatial location of the initial pointing (before scanning) for both the forward and reverse scans.

Pairs of (`POSTARG1`, `POSTARG2`) took exactly two unique pairs of values, which `Arctor` stores to identify the corresponding indices for forward and reverse scan directions. For our WASP-43b eclipse observation, we concluded that forward scan trace images began with `POSTARGS`:[−53.459629, −36.240479], and reverse scan trace images began with `POSTARGS`:[−73.743279, −37.577122]. These values are unique to each individual observation but are static values throughout each visit.

Cosmic-Ray Rejection

We performed cosmic-ray rejection with σ outlier estimation over the temporal axis, i.e., cycling through each pixel, computing the median and standard deviation along the time axis. Any values above 5σ from the median were flagged as cosmic rays. We then set those pixels to the temporal median. Although there is an integrated separation of ∼344 ppm between the forward and reverse scans in the time series, the median flux variation over time was ∼10% per column, which is several orders of magnitude greater than the ppm separation between forward and reverse scans. As such, `Arctor` performed the cosmic-ray rejection over the pixel-by-pixel light curves without considering scan direction.

Trace Position and Angle

To derive the y-center position of each trace in our images, `Arctor` fit a 1D Gaussian to all 951 columns in each of the 75 frames using the `Astropy` package;[28] `Astropy` is a standard astronomical functions library (Astropy Collaboration et al. 2018; Virtanen et al. 2020). We then fit a straight line to the collection of 1D Gaussian mean values for each frame (over the trace columns only) using linear least-squares regression. Only the mean values for 1D Gaussian fits over the illuminated part of the trace were used in determining the center position and angle (see below).

`Arctor` stored the intercept from this straight line fit as the y-center position for each trace and the slope as the rotation angle of the trace. We later used the rotation angle in the photometry and sky background procedures (below) for the theta rotation of the rectangular aperture inside the `Photutils` package (Bradley et al. 2019). Figure 11 shows the necessity and accuracy of measuring the trace rotation angle for narrow apertures. Although our best AICc and BIC aperture used a much larger height and width than shown here, the effect of modeling the angle of the trace improved the photometric stability of our light curves by ∼0.5%, i.e., ∼10 ppm SDNR over the light curve.

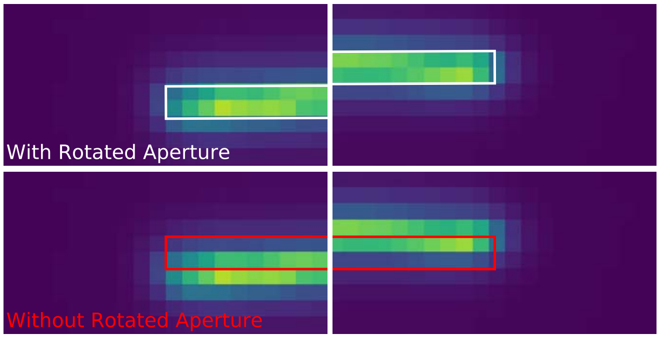

Figure 11. Effect of measuring the trace rotation angle. The necessity and accuracy of measuring the trace rotation angle for narrow apertures is apparent. Although our best AICc and BIC aperture used a much larger height and width than shown here, the effect of modeling the angle of the trace improved the photometric stability of our light curves by ∼1% (i.e., 5–10 ppm SDNR).

The y-positions in the first orbit are offset by ∼0.1 pixels, or 10× the interorbit scatter of the y-positions, compared to the three remaining orbits (see Figure 12). We later derived a meaningful correlation between the y-positions and the flux measured that our AICc and BIC analysis determined was necessary to select the "best" model+light curve pair, implying that including the first orbit in our observations provided improved the SDNR over the full eclipse observation.

`Arctor` derived the x-center positions by integrating each image in a very narrow subframe that included the trace: a 10×951 pixel window. By integrating down the column within each subframe, the code derived a 1D representation of the trace (integrated flux versus pixel). After this, we created a cubic spline to oversample the trace by a factor of 100. `Arctor` then measured where the integrated trace reached >50% of its own maximum value on the left and right edges. It stored the x-center positions as the midpoint between the left and right edges of the 1D trace. We later determined that this feature vector was critical in reducing correlated noise sources between the forward and reverse scanned images.

Investigating Correlations between Positions and Flux

After performing a simple integration to estimate the flux (i.e., sum(frame—median(frame))) over time, we discovered a difference in the flux read from reverse scanned images compared to the forward scanned images. The separation in median flux measurements between reverse and forward scans is ∼344 ppm. This could be attributable to differential flat-fielding errors encountered by the trace encompassing slightly different pixels during the forward and reverse scans (i.e., <0.5 pixel difference). Figure 13 shows the position of all 75 HST WFC3/UVIS images taken during our observations. There is a clear separation of $\sim\frac{1}{2}$ pixel in the x-center position between the forward and reverse scanned images. There is also an apparent shift in the y-center positions during the first orbit.

The difference in flux could also be related to the lack of a shutter, which would cause extra flux to be read by the detector in one of the scan directions. Specifically, because WFC3 does not have a shutter, there is a slight variation in the exposure time that depends on whether the scan direction is upstream or downstream relative to the detector readout direction. Examining the trace length versus scan direction (see Figure 17 below), we noted that reverse scanned images sustained longer traces

---

[27] github.com/exowanderer/exomast_api

[28] astropy.org

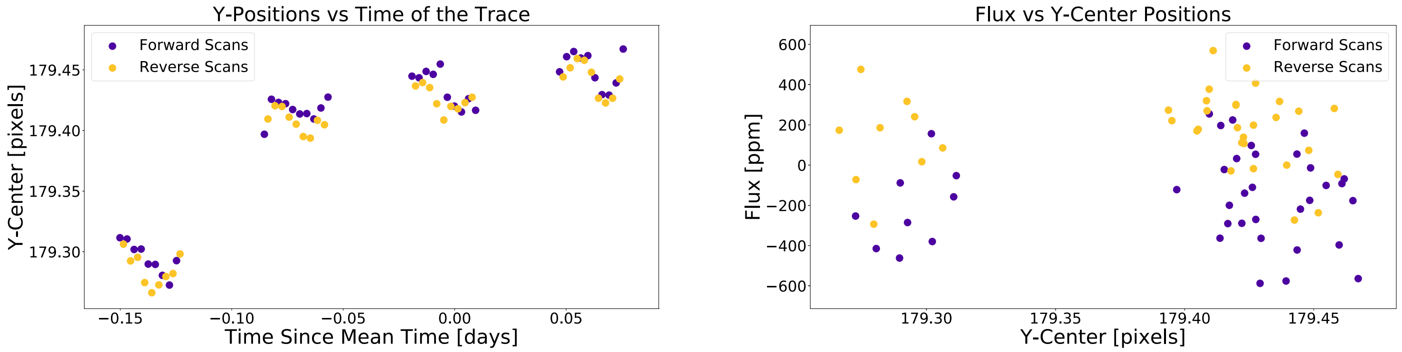

Figure 12. (Left) The y-center position of our WASP-43 HST WFC3/UVIS observations over four HST orbits. The first orbit sustained y-center positions significantly different from the three following orbits. (Right) Our AICc/BIC model selection process diagnosed a meaningful linear correlation between the flux and the y-center positions.

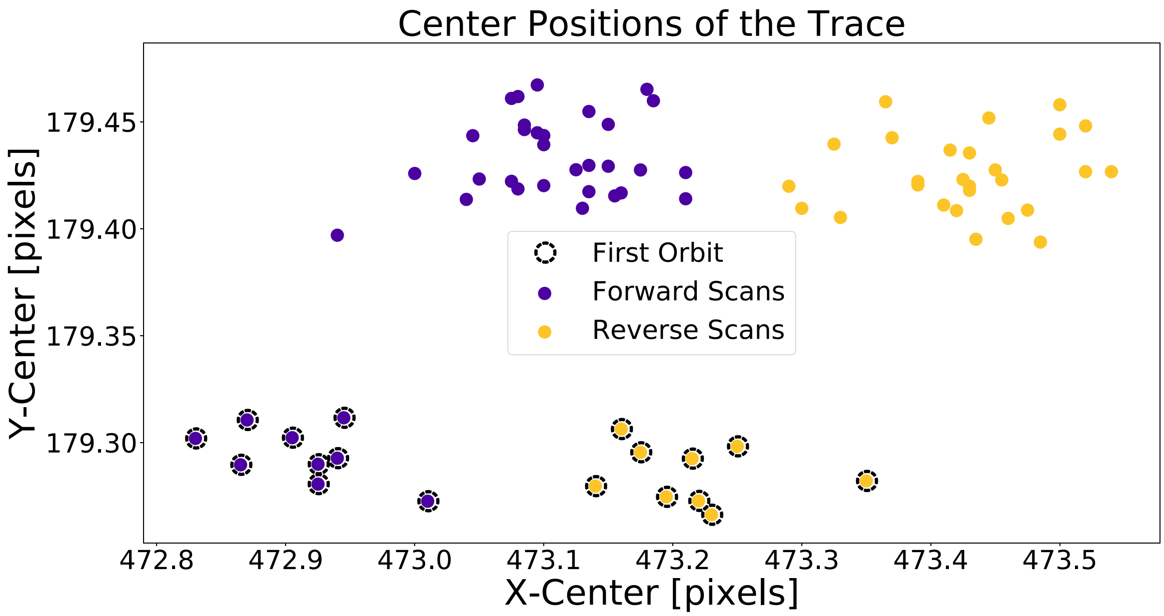

Figure 13. The x- and y-center positions of the trace during all 75 images taken with HST WFC3/UVIS for our WASP-43b eclipse observations. There is a clear separation of $\sim\frac{1}{2}$ pixel in the x-center position between the forward and reverse scanned images; there is also a small but significant shift in the y-center positions during the first orbit, as discussed above.

by ∼0.2 pixels, as compared to the forward scanned images. We accounted for each of these factors in our MAP and MCMC analyses, using linear models for all five possible parameters (see Section A.1 below).

Median Sky Background

Our purpose here is to measure the integrated background flux inside a rectangular annulus centered on the trace and rotated to match the trace. We later compare these results with the column-wise sky background estimates (see below).

After measuring the x/y-centers and rotation of the trace, we used a rectangular aperture to include the flux from the scan while minimizing the background flux included. The inner aperture was 542 pixels wide by 225 pixels high; the outer aperture was 617 pixels wide by 375 pixels high. We chose these values to be far outside of the stellar flux (which extends 25 pixels in all directions from the trace) and avoid edge effects that may occur within ∼10 pixels of the edge of the detector. Figure 2 shows the exact aperture sizes and relative locations used in measuring both the background sky values and the photometric light-curve flux values.

By integrating over the two apertures and then subtracting the medium aperture integration from the larger aperture integration, `Arctor` generated a mean sky background estimate. In the `Photutils` package, there is a `rectangular annulus` function (Bradley et al. 2019), but it makes assumptions about the ratio between the inner and outer height relative to the inner and outer width that we found did not include enough valuable background real estate. The result was an average background level of 15.2 e^{-} pixel^{-1}.

Column-wise Sky Background

Because our observations use the HST scanning mode, there remains the possibility that the background can change as a function of column number (in the scan direction) as a function of either flat-field errors or scattered light that is also being scanned along the image. As such, `Arctor` computed both the median and column-wise sky background estimate.

For the column-wise sky background estimation, we used a column-wise aperture for its mask over each image. We selected the column-wise aperture to include all pixels that are 150 rows above and below the trace but not the 10 pixels at the edge, as recommended by the HST scanning mode suggested

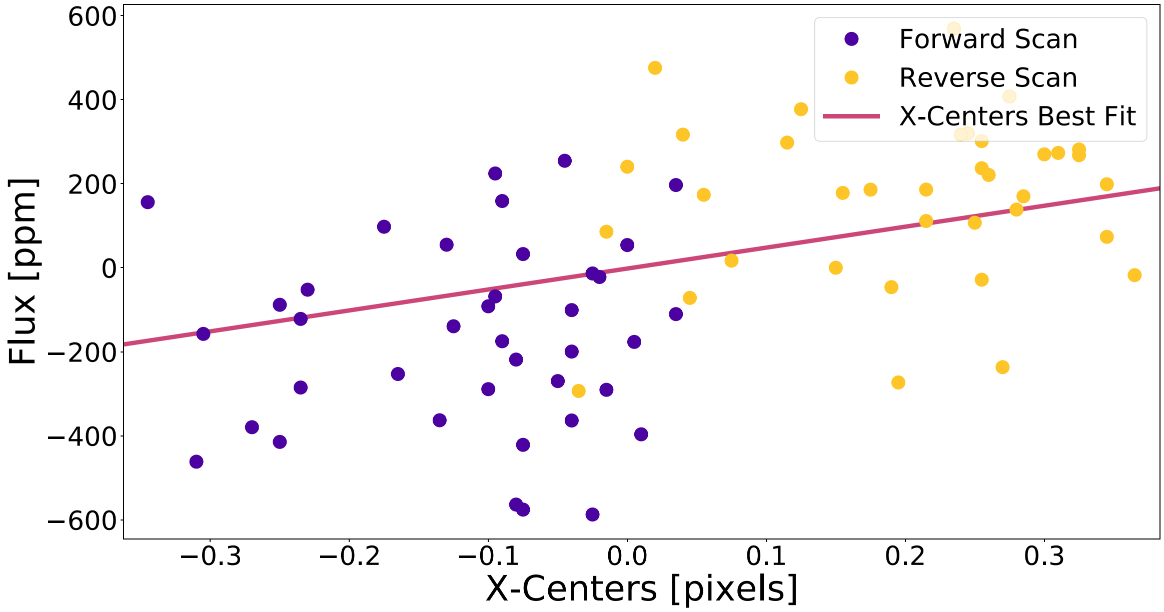

Figure 14. The 2D linear correlation between time + x-center positions and normalized flux for our (AICc) "best" light curve. The slope values are relative to the standard deviation of the flux and pixel coordinates (over the full observation). As before, we coded the forward scan values in violet and reverse scan values in orange.

reduction pipeline. It stored the 951 median values, taken down the masked columns, as the column-wise sky background vectors per frame. We did not rotate the column-wise integration to match the trace angle in favor of a "straight down the columns" median. The column-wise background estimates averaged closer to 19.5 e^{-} pixel^{-1}. The values included structure ranging from 10 e^{-} at the left edge, to 26 e^{-} in the region above/below the trace, to 12 e^{-} at the right edge.

After computing our initial 800 photometry estimates with both the median and column-wise sky background (1600 photometric estimates combined), we found that the rms for both background estimates found equivalent values. As such, we chose to move forward with the column-wise sky background estimates because they seemed to follow the physical trend of the light on the detector (i.e., larger in the middle and smaller on the edges).

Estimating the Light Curves: Photometry

To integrate the flux received from the host star WASP-43 before, during, and after the eclipse, `Arctor` used the `rectangular aperture` function to sum over all rows and columns within `aper-width` and `aper-height` pixels around the trace (see Figure 2). The apertures were centered on the trace center and rotated to match the rotation of the trace (see Figure 11).

Coarse-grain Photometry

We ranged our coarse-grain values for `aper-width` and `aper-height` at 1–100 and 1–300, respectively, each encompassing 20 samples; thus, the coarse-grain `aper-width` and `aper-height` spacing was set to 5 and 15 pixels, respectively. This created 400 light curves that we used to determine the best set of values to center our fine-grain photometry (see below). Via the standard deviation of raw flux, we computed the scatter along the integrated time series as our metric to select the center and range of our (below) fine-grain `aper-width` and `aper-height` values. While grid searching over both fine- and coarse-grain photometry, we included a range of aperture widths and heights, from 1 up to 400 pixels outside the trace.

Fine-grain Photometry

The coarse-grain span of the photometric light curves revealed that `aper-width` and `aper-height` values of 21 × 51, respectively, resulted in the minimum scatter (std-dev) of 206 ppm. As a result, we recomputed 400 new light curves with `aper-width` and `aper-height` values spanning 11–31 and 41–61, respectively, encompassing 20 samples in each parameter; thus, the fine-grain `aper-width` and `aper-height` spacing was set to 1 pixel. These integrations also found the "best" light-curve scatter of 206 ppm but with `aper-width` and `aper-height` values of 13 × 45. This is the light curve that we show in Figures 1 and 4.

MAP

Using the `exoplanet`[29] package, we fit 32 models to each of the 400 light curves, culminating in 12,800 model fits. The 32 models were 2^5 toggles for every possible combination of whether to simultaneously fit a linear trend to any of our five systematic features: forward/reverse indices, x-centers (Figure 14), y-centers (Figure 15), trace angles (Figure 16), and trace lengths (Figure 17). We analyzed our extracted data set of AICc/BIC results per MAP fit to select the best model, which minimized both AICc and BIC. Note that a linear trend was fit to the time feature in all cases; this temporal variation can be attributed to long-term variation in the sensitivity or flat-field error or the stellar variability, if significant enough.

In Appendix B, we show the result of all 12,800 models compared across SDNR, χ^2, AICc, and BIC. In the AICc and BIC case, the global picture and "best" model selected were identical, i.e., a "13 × 45" rectangular aperture. Moreover, linear fits to x-center, y-center, and trace length resulted in the minimum AICc and BIC light curve with SDNR= 72 ppm; see Figure 4. The cohesion between complementary information criteria strongly implies that our model selection process is valid and sound.

MCMC Posterior Estimation

---

[29] https://github.com/dfm/exoplanet

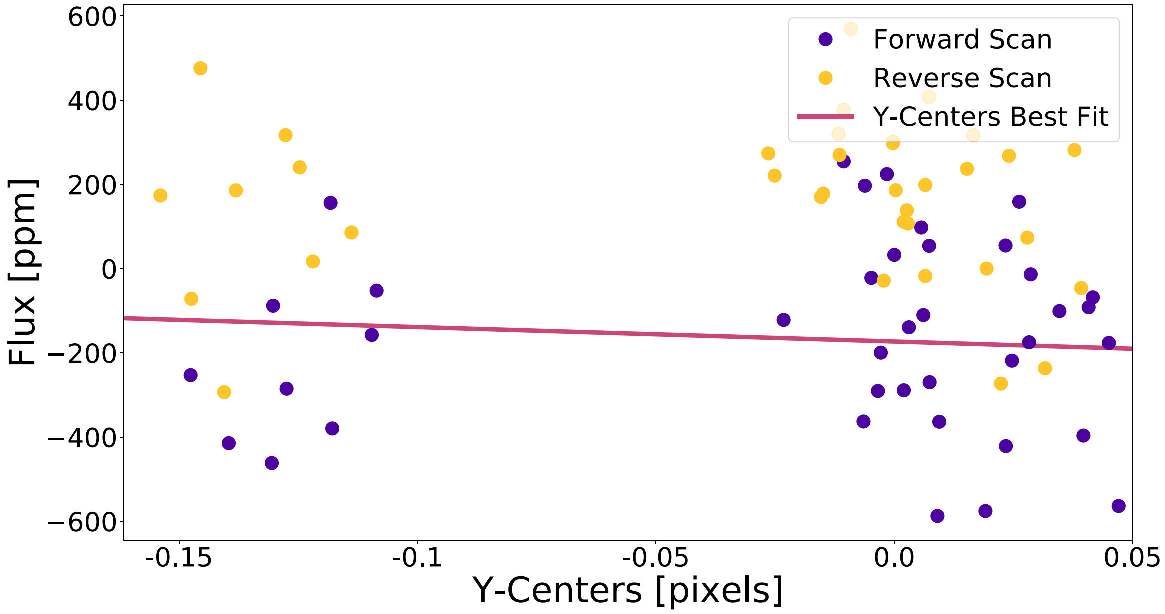

Figure 15. The 2D linear correlation between time + y-center positions and normalized flux for our (AICc) "best" light curve. The slope values are relative to the standard deviation of the flux and pixel coordinates (over the full observation). As before, we coded the forward scan values in violet and reverse scan values in orange.

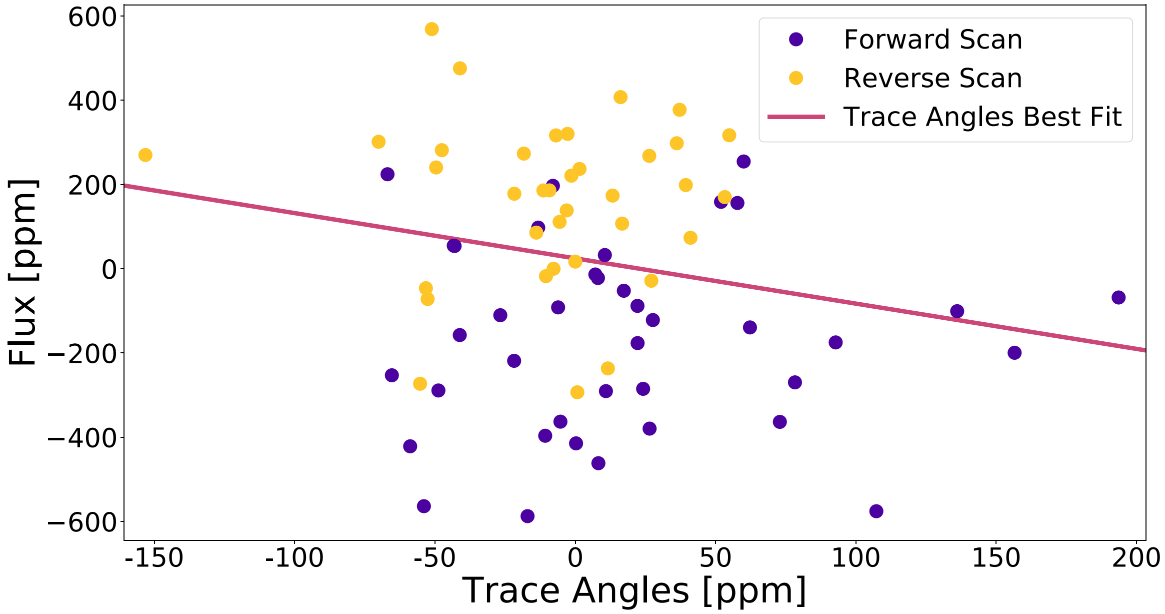

Figure 16. The 2D linear correlation between time + trace angles and normalized flux for our (AICc) "best" light curve. The slope values are relative to the standard deviation of the flux and pixel coordinates (over the full observation). As before, we coded the forward scan values in violet and reverse scan values in orange.

To extract the greatest information content, we used a collection of 16 HMC estimates using linear and nonlinear models. We sampled 3000 *tune* steps and 3000 *draw* steps for all 16 chains and each of the 25 light curves examined with this HMC; increasing the tune/draw counts did not change the results. We used a lognormal prior for the mean offset and eclipse depth and a wide normal prior for the four slope parameters that fit as well: slopes over the time, x-center, y-center, and trace length features. We also tested a log-uniform and uniform prior over the eclipse depth. After sampling 16 chains for each of the 25 light curves, we used the autocorrelation timescale and Gelman–Rubin test, as provided by the `exoplanet` package (Foreman-Mackey et al. 2020). This package includes an analytic transit model (`BATMAN`; Kreidberg 2015) and a spherical harmonic phase-curve model (STARRY; Luger et al. 2019).

Figure 3 shows the 2D MCMC correlation plots (i.e., corner plot) from our best AICc and BIC selected model + lightcurve pair. This best-fit model in Figure 3 included fits for the `Mean`, `Edepth`, `Slope`, `Slope Xcenter`, `Slope Ycenter`, and `Slope Trace Length`. The slopes in this model were generated from the simultaneous, linear fits to the corresponding features, with a single, unified "intercept" represented by the mean. The results clearly show that the slopes in each of the three feature spaces were significantly detected and contributed to the quality of the final SDNR, i.e., their

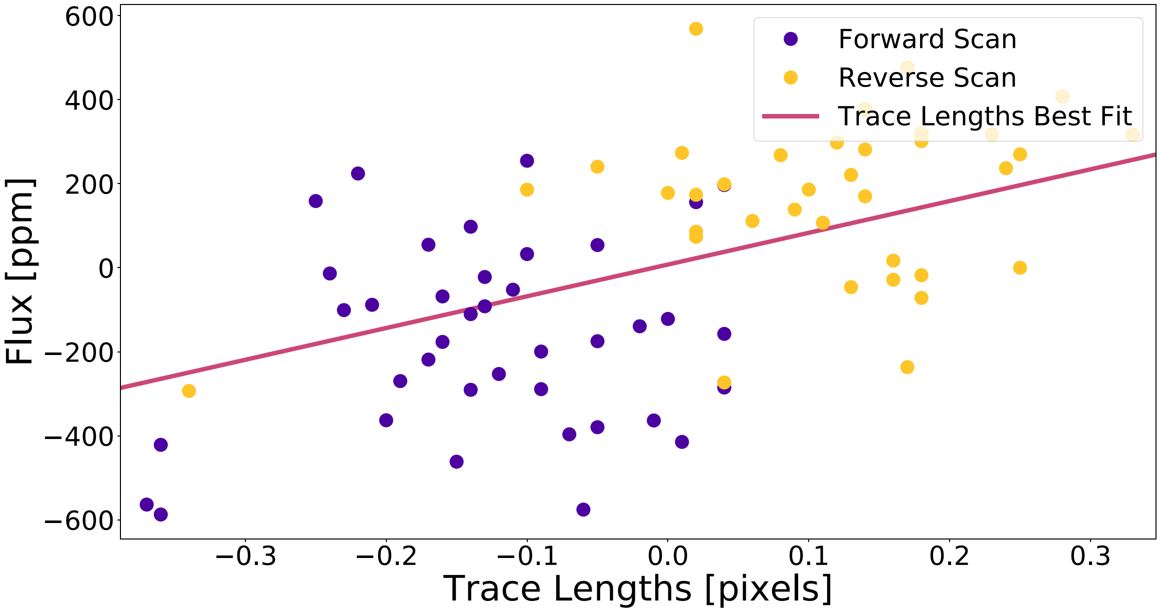

Figure 17. The 2D linear correlation between time + trace lengths and normalized flux for our (AICc) "best" light curve. The slope values are relative to the standard deviation of the flux and pixel coordinates (over the full observation). As before, we coded the forward scan values in violet and reverse scan values in orange.

posterior distributions are bounded. In contrast, the eclipse depth was not detected—with a 3σ upper limit of 67 ppm—because a significant portion of the posterior includes the physical minimum of zero eclipse depth.

Although we do not show this here, we also fit to the eclipse depth with a uniform and log-uniform prior. The log-uniform prior also derived a nondetection with a peak around $\log 10(\text{eclipse depth}) \sim -20$, i.e., an eclipse depth of $\sim 10^{-20}$. Unfortunately, the log-uniform prior appeared to be more strongly influenced by the exact bounds of the prior; i.e., the MAP would vary from a $\log 10(\text{eclipse depth})$ of -100 to -10, depending on the selected prior boundaries. In contrast, the uniform prior for the eclipse depth provided consistent results across all of our trials and selections for the prior boundaries.

A.1. HST WFC3/UVIS Scanning Mode Correlated Noise

In order to diagnose any plausible connections between the measured flux and non-astrophysical noise sources, we examined a suite of linear trends between the flux measurements and the time values, *x*-center positions, *y*-center positions, trace angles, and trace lengths, as seen in Figures 14–17, respectively. These figures show initial estimates for 2D linear correlations between the normalized flux and the four input vectors for our systematics analysis. That is, we fit a plane to the features, including time in all four fits, while alternating the other four features listed above.

We also examined the effect of fitting two distinct means for flux values corresponding to the forward and reverse indices, i.e., a mean_{rev} fit to the orange points in Figure 1 and a mean_{fwd} fit to the violet points in Figure 1. When considering separated mean flux values, we fit for the one set of eclipse parameters and slope values over each systematic feature. These fits included the 2^5 combinations, mentioned above, in our AICc and BIC model selection process.

The most significant linear trend that we detected from only time + feature versus flux resulted from bilinear fitting with *x*-center position and time value features compared to normalized flux estimates. Note that Planar2D is a plane model (i.e., bilinear; $\text{flux} = a \times \text{time} + b \times \text{other}$) for use with fitting routines.

Figures 14–17 only show our initial estimates from our fits. Our final AICc and BIC and parameter estimates were generated using the combination of MAP and BCR analysis, both sourced from the `exoplanet` package (XO; Foreman-Mackey et al. 2020).

Using the XO package, we were able to test 12,800 model + aperture configurations, i.e., 32 models with 400 rectangular aperture estimates of the light curve for various aperture widths and heights. We provide a descriptive visualization of these 12,800 model results over our information criteria–based model selection techniques in Appendix B. The result of this analysis revealed that the "best-fit model" resulted in a minimum $\text{AICc} = 148$ and $\text{BIC} = 146$, with $\Delta\text{AICc} = \Delta\text{BIC} = 2$, which is considered a significant decrease (Schwarz 1978; Schöniger et al. 2014).

Appendix B
Comparative MAP + AICc Analysis over Linear Correlations

B.1. Linear Models

To select between our 12,800 model + light curve pairs (i.e., parameters + hyperparameters), we computed the AICc and BIC for each of our options. We then chose the option with the minimum AICc and BIC. This model resulted from the same model option, which was not guaranteed a priori. Here we describe our process and the underlying considerations when using AICc and BIC for model selection.

The AICc is the corrected Akaike information criterion, and the BIC is the Bayesian information criterion. Both information criteria are sufficient metrics for model selection when comparing analytic, quasi-linear models. Both criteria penalize the log-likelihood function ($\log L$) by the number of parameters

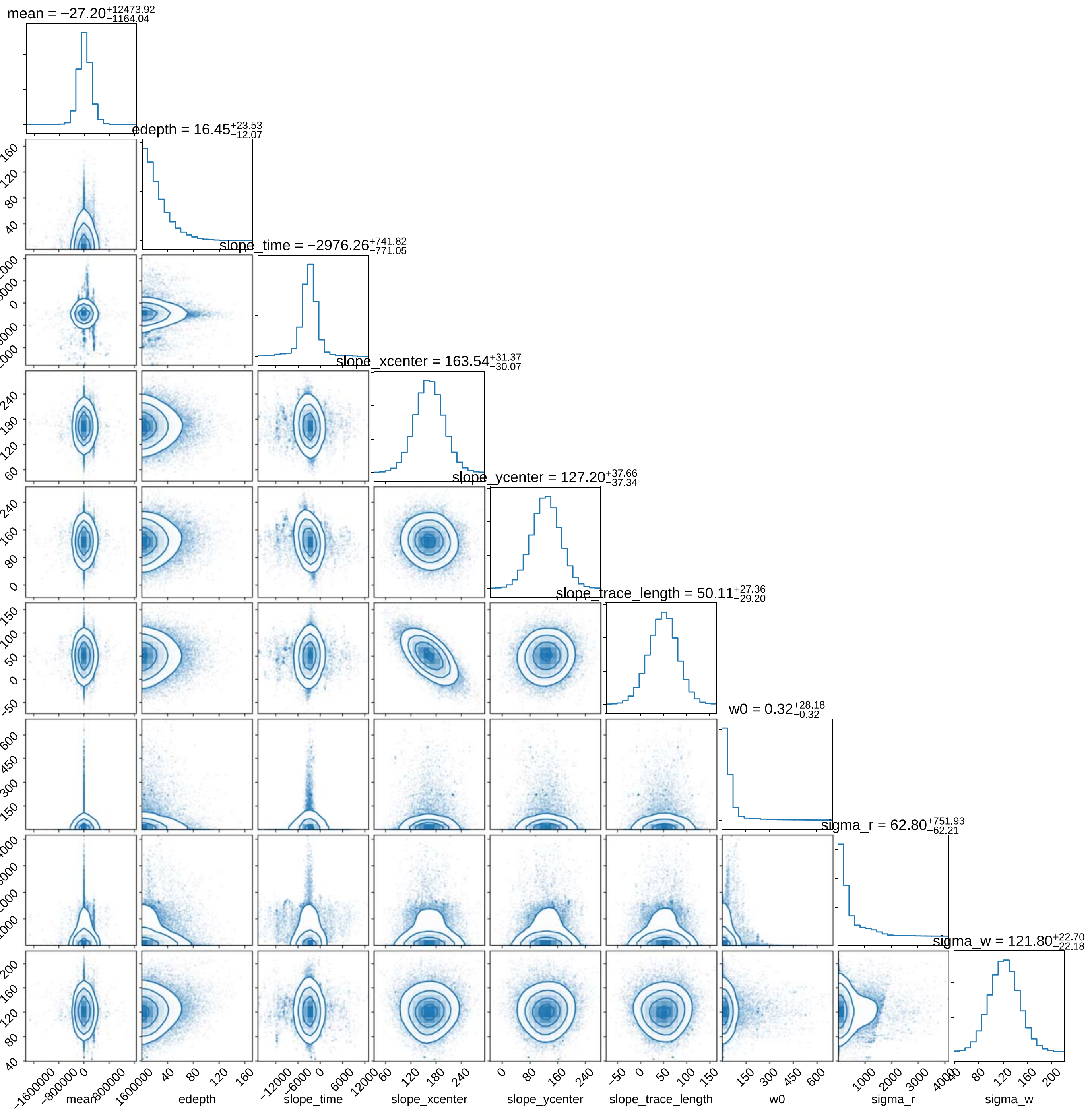

Figure 18. Correlation ("corner") plot for our reanalysis using GPs. From personal communications with the `exoplanet` development team (https://github.com/exoplanet-dev/exoplanet/issues/76), we used their built-in GP methods (i.e., `celerite`) to create a GP that would probe the autocorrelation timescales and amplitudes for nonlinear correlated noise in our residuals. We simultaneously sampled the linear slopes for time, x-center, y-center, and trace lengths (same as our best model above), along with the GP kernel hyperparameters: σ_r, σ_w, and ω_o. The result is twofold: (1) the posterior for σ_r is significantly skewed, with a median of 63^{+751}_{-62} ppm, and (2) the AICc/BIC increased by $\Delta\text{AICc} \sim \Delta\text{BIC} > 10$. Both results reject the hypothesis that power-law noise is measurable within our residuals.

(k) relative to the number of samples (n), i.e.,

$$\text{BIC} = -2\log L + k\log n$$

$$\text{AICc} = -2\log L + k + \frac{2k(k+1)}{n-k-1}.$$

Each equation is an approximation to the Bayesian evidence under very specific linear and/or Gaussian conditions (Schöniger et al. 2014). The AICc is corrected for usage with a finite number of data points, i.e., "small" data sets. These criteria provide a more robust estimate for the goodness of fit than the SDNR or χ^2, the latter being a simplified representation of the log-likelihood ($\log L$ above) under the assumption that the posterior approximates a Gaussian normal distribution.

We used the AICc and BIC to select which of the 32 models (i.e., parameters) and 400 light curves (i.e., hyperparameters)

Table 2
The Set of 16 Linear Models Tested for Our Analysis

Model Features	Number of Parameters
Time + eclipse + offset	3
Time + eclipse + offset + *X*-centers	4
Time + eclipse + offset + *Y*-centers	4
Time + eclipse + offset + trace angles	4
Time + eclipse + offset + trace lengths	4
Time + eclipse + offset + *X*-centers + *Y*-centers	5
Time + eclipse + offset + *X*-centers + trace angles	5
Time + eclipse + offset + *X*-centers + trace lengths	5
Time + eclipse + offset + *Y*-centers + trace angles	5
Time + eclipse + offset + *Y*-centers + trace lengths	5
Time + eclipse + offset + trace angles + trace lengths	5
Time + eclipse + offset + *X*-centers + *Y*-centers + trace angles	6
Time + eclipse + offset + *X*-centers + *Y*-centers + trace lengths	6
Time + eclipse + offset + *X*-centers + trace angles + trace lengths	6
Time + eclipse + offset + *Y*-centers + trace angles + trace lengths	6
Time + eclipse + offset + *X*-centers + *Y*-centers + trace angles + trace lengths	7

Note. We used all 32 possible combinations of these features and only in the linear model; see equation below. Time + eclipse + offset was our simplest model. Moreover, each of these models was also fit with or without separating the data set into forward and reverse scanned independent but linked subsets. This resulted in 16 models without separating into forward and reverse scans + 16 models with separating into forward and reverse scans.

provided the best representation of the data. The best model + light curve pair achieved the smallest AICc or BIC by at least a ΔBIC/AICc of 2 (Schwarz 1978; Schöniger et al. 2014).

Each of our models included up to five linear parameters + the eclipse depth, i.e.,

$$\begin{aligned}\text{flux} &= a \cdot \text{time} + b \cdot \text{x}{-}\text{center} + c \cdot \text{y}{-}\text{center}\\ &\quad + d \cdot \text{trance length}\\ &\quad + e \cdot \text{trance angle} + \text{eclipse model} + \text{offset}.\end{aligned}$$

The best AICc and BIC result was achieved using a linear fit to four features: time, *x*-center position, *y*-center position, and trace length. The following figures show the distribution of AIC, BIC, SDNR, and χ^2 over each of our 12,800 models. The important factors to see are that the minimum SDNR (Figure 19) and χ^2 (Figure 20) are always achieved by the model with the most parameters (i.e., upper left panel) to achieve the least rms scatter, while the AICc (Figure 21) and BIC (Figure 22) select the model with a balance between the number of parameters and the complexity of the model, i.e., with an AICc = 148 and a BIC = 146. (Note that those AICc and BIC values cannot be compared directly to each other.)

B.2. Autocorrelated Noise

After selecting the model configuration that minimized the AICc and BIC, we further investigated the possible presence of autocorrelated noise, i.e., "power-law noise" with PSD $(\omega) \sim \omega^{-\beta}$ (Pont et al. 2006; Cubillos et al. 2017). We attempted several power-law noise procedures (see below) and included them in the `Arctor` package, but only the GP analysis produced reproducible MCMC results (Foreman-Mackey et al. 2017, 2020).

Carter & Winn (2009) derived a wavelet analysis technique for transiting exoplanet observations with the Spitzer Space Telescope that introduced the terminology σ_r to represent the amplitude of residual power-law noise and σ_w to represent the underlying white noise in the residuals. That algorithm specifically mitigates "pink noise" (i.e., PSD $(\omega) \sim \omega^{-1}$) and requires evenly spaced data with high cadence and many samples. Carter & Winn (2009) and Cubillos et al. (2017) discussed several other techniques to mitigate various power-law noise effects; they also focused on high-cadence transit observations with the Spitzer Space Telescope. Because of HST's large duty cycle and gaps for Earth's eclipse, our data do not satisfy the underlying assumptions that would allow these techniques to be effective. As such, we chose to implement a GP regression technique that is designed to identify nonperiodic autocorrelated noise signatures in residual data (Gibson et al. 2012a, 2012b; Foreman-Mackey et al. 2017). More directly, we used the implementation of `celerite` that was built into `exoplanet`[30] (Foreman-Mackey et al. 2017).

Using a simple harmonic oscillator kernel with the `celerite` package,[31] we modeled the autocorrelated noise with a covariance matrix kernel shape,

$$k(\tau) = S_o \omega_o \exp^{-\frac{\omega_o \tau}{\sqrt{2}}} \cos\left(\frac{\omega_o \tau}{\sqrt{2}} - \frac{\pi}{4}\right),$$

which obeys the power-law relationship

$$S(\omega) = \sqrt{\frac{2}{\pi}} \frac{S_o \omega_o^4}{\omega^4 + \omega_o^4} \sim \omega^{-4} \text{ for large } \omega.$$

We represent $\sigma_r = S_o \omega_o^4$ as the the amplitude of the power-law noise. We also use an error scaling term, σ_w, along the diagonal of the covariance matrix: $\sigma_{\text{data}}^2 + \sigma_w^2$.[32] Furthermore, we sample the GP kernel hyperparameters from wide lognormal priors, $\log(\sigma_r) \sim \mathcal{N}(0, 15)$ and $\log(\sigma_w) \sim \mathcal{N}(0, 15)$, which created lognormal distributions from $(0, \infty)$ centered at unity.

We simultaneously fit the time, *x*-center, *y*-center, trace length, and offset linear models with the GP kernel hyperparameters to constrain the BCR over the new, nonlinearly extended model. We provide a correlation plot for comparison in Figure 18, which shows that the posterior over the power-law amplitude is significantly skewed and consistent with zero (the null hypothesis):

$$\sigma_w = 122 \pm 23 \text{ ppm} \quad \sigma_r = 63^{+752}_{-62} \text{ ppm}.$$

Moreover, if we consider the three hyperparameters of our kernel to be congruent with the three to seven parameters of our parametric models (see Table 2), then we also conclude that introducing the GP significantly increases the AICc and BIC by ΔAICc ∼ ΔBIC > 10. Altogether, we reject the hypothesis that autocorrelated noise exists in our residuals. We further reexamined 6400 of our best non-GP included models by adding the same GP covariance matrix above. We computed the MAP (not MCMC) for each of them and also found that the use of GPs is not warranted within the uncertainties for our residuals.

---

[30] https://github.com/exoplanet-dev/exoplanet

[31] https://github.com/dfm/celerite

[32] https://github.com/exoplanet-dev/exoplanet/issues/76

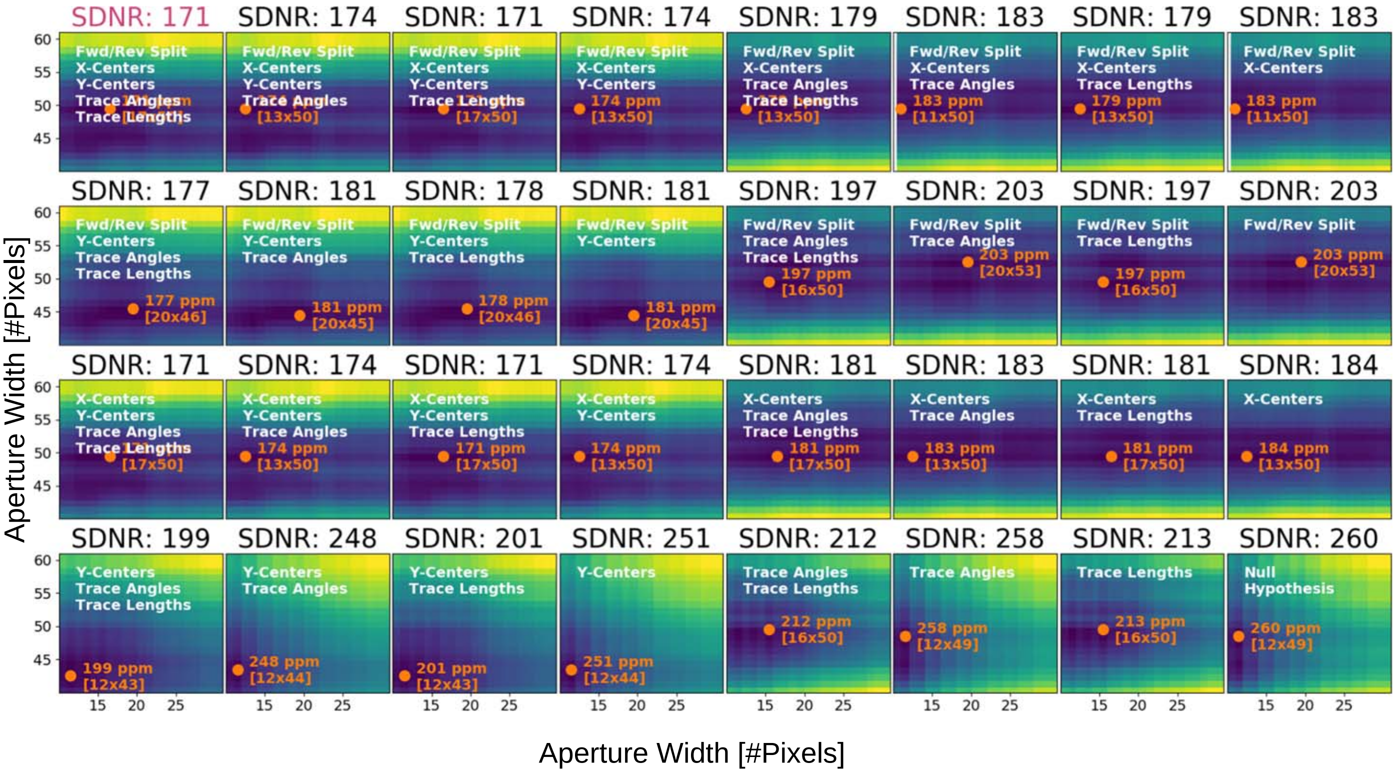

Figure 19. The 12,800 MAP results compared to SDNR. The SDNR will almost always choose the model with the largest number of parameters. This can be seen by the minimum SDNR achieved in the upper left panel: SDNR = 171. We use AICc and BIC to avoid falling into models that do not extrapolate well.

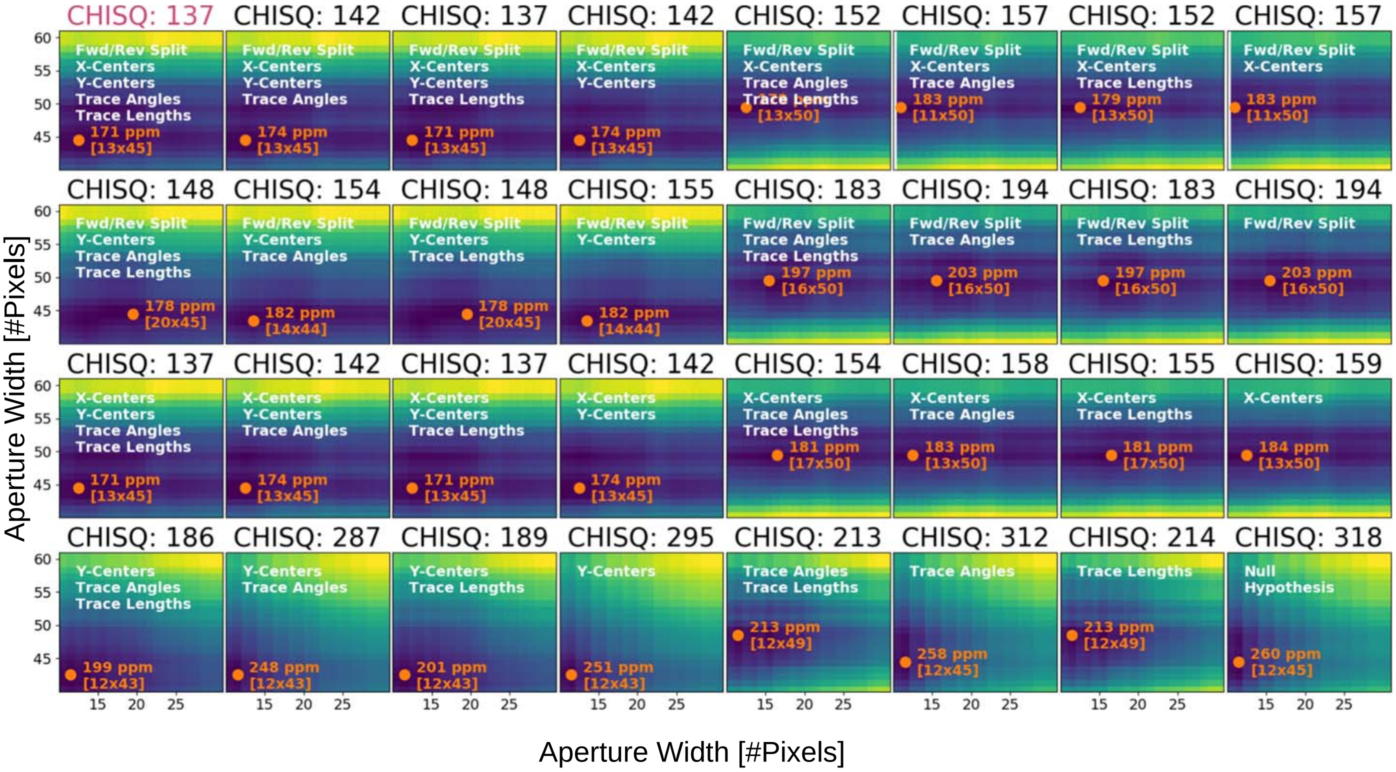

Figure 20. The 12,800 MAP results compared to χ^2. Much like SDNR, χ^2 will almost always choose the model with the largest number of parameters. This can be seen by the minimum χ^2 achieved in the upper left panel: $\chi^2 = 137$. We use AICc and BIC to avoid falling into models that do not extrapolate well.

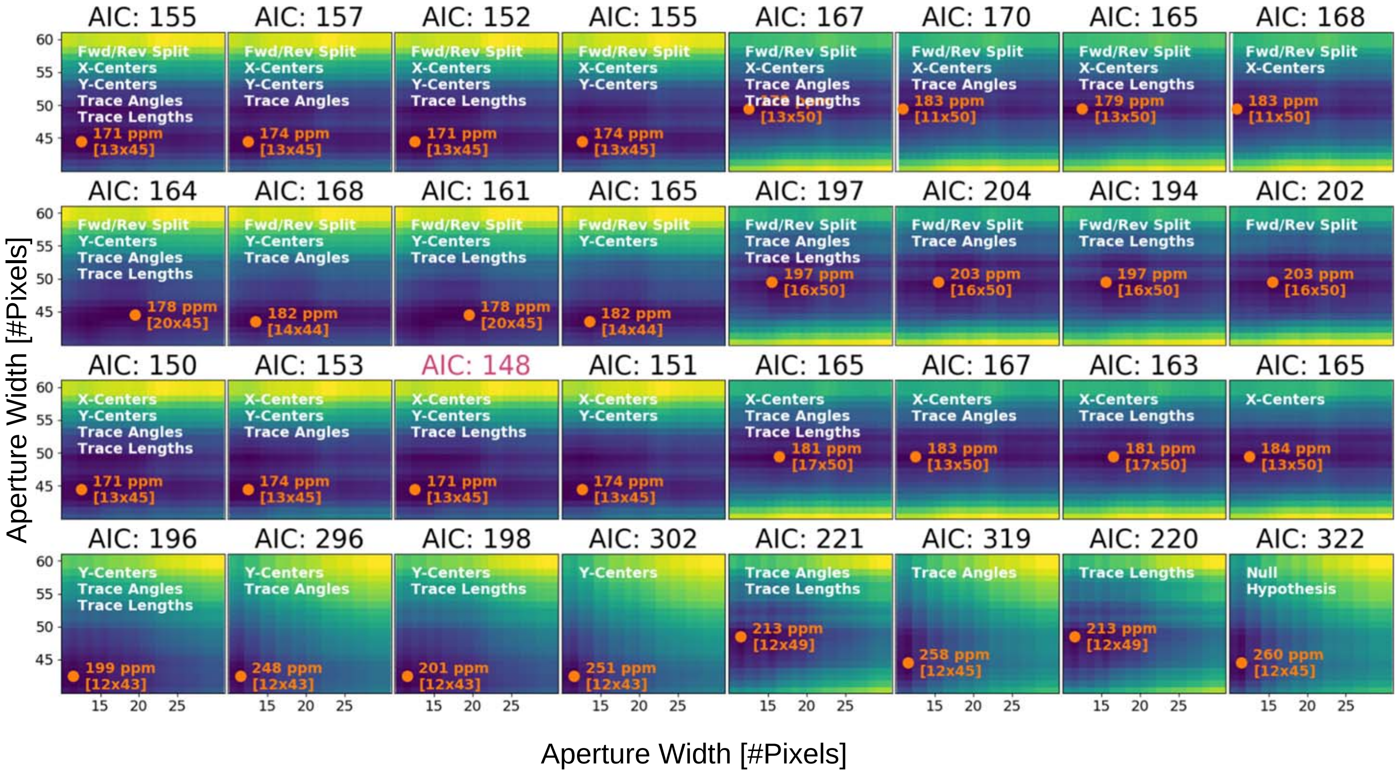

Figure 21. The 12,800 MAP results compared to AICc. Unlike like SDNR or χ^2, AICc will only choose the model with the largest number of parameters if it also minimizes the complexity of the data set. This can be seen by the minimum AIC achieved in (row, column) = (3, 3) (starting from upper left), AIC = 148.

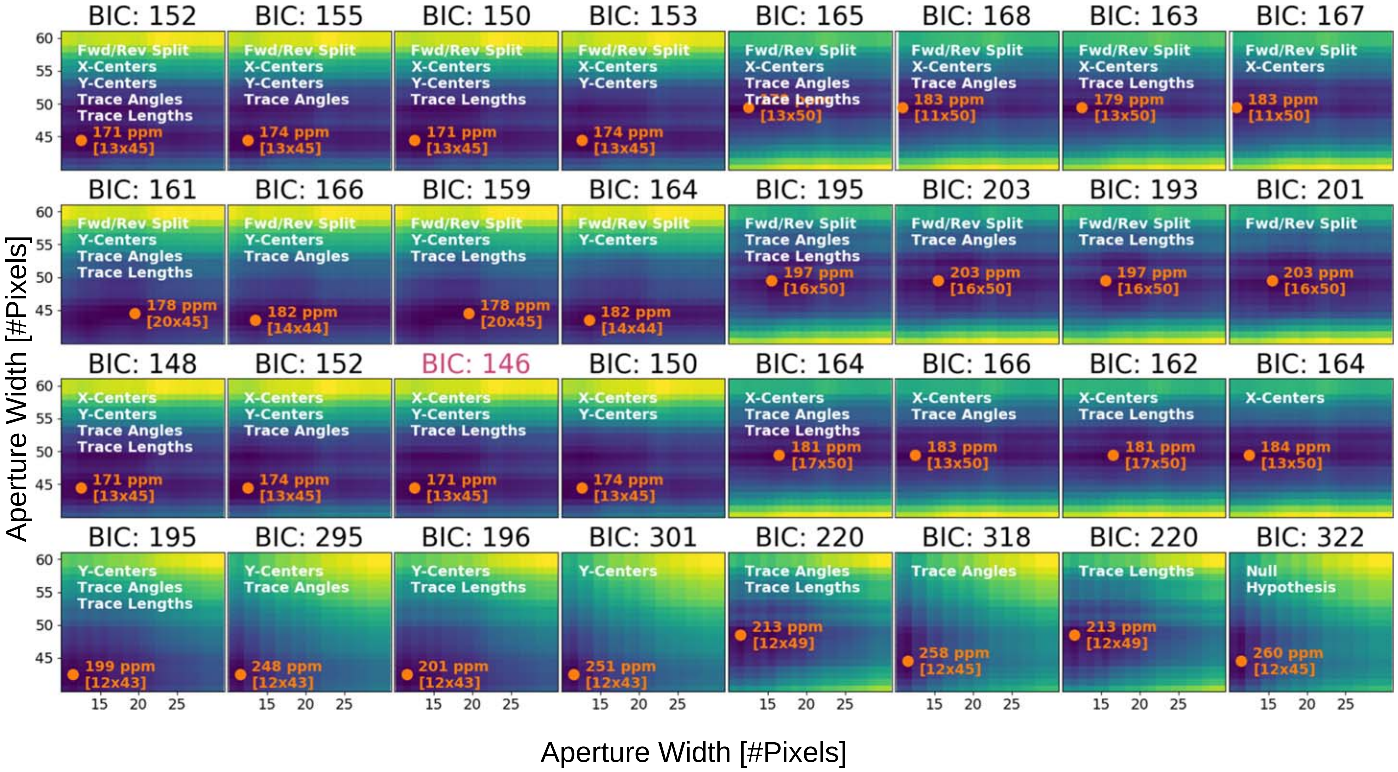

Figure 22. The 12,800 MAP results compared to BIC. Unlike like SDNR or χ^2, BIC will only choose the model with the largest number of parameters if it also minimizes the complexity of the data set, the same as AICc. This can be seen by the minimum BIC achieved in (row, column) = (3, 3) (starting from upper left), BIC = 146.

ORCID iDs

Jonathan Fraine https://orcid.org/0000-0003-0910-5805
L. C. Mayorga https://orcid.org/0000-0002-4321-4581
Kevin B. Stevenson https://orcid.org/0000-0002-7352-7941
Nikole K. Lewis https://orcid.org/0000-0002-8507-1304
Tiffany Kataria https://orcid.org/0000-0003-3759-9080
Jacob L. Bean https://orcid.org/0000-0003-4733-6532
Giovanni Bruno https://orcid.org/0000-0002-3288-0802
Jonathan J. Fortney https://orcid.org/0000-0002-9843-4354
Laura Kreidberg https://orcid.org/0000-0003-0514-1147
Caroline V. Morley https://orcid.org/0000-0002-4404-0456
Nelly C Mouawad https://orcid.org/0000-0003-1609-5625
Kamen O. Todorov https://orcid.org/0000-0002-9276-8118
Vivien Parmentier https://orcid.org/0000-0001-9521-6258
Hannah Wakeford https://orcid.org/0000-0003-4328-3867
Y. Katherina Feng https://orcid.org/0000-0002-5032-5060
Brian M. Kilpatrick https://orcid.org/0000-0003-4220-600X
Michael R. Line https://orcid.org/0000-0002-2338-476X

References

Ackerman, A. S., & Marley, M. S. 2001, ApJ, 556, 872
Allart, R., Bourrier, V., Lovis, C., et al. 2019, A&A, 623, A58
Allart, R., Lovis, C., Pino, L., et al. 2017, A&A, 606, A144
Angerhausen, D., DeLarme, E., & Morse, J. A. 2015, PASP, 127, 1113
Astropy Collaboration, Price-Whelan, A. M., Sipőcz, B. M., et al. 2018, AJ, 156, 123
Astropy Collaboration, Robitaille, T. P., Tollerud, E. J., et al. 2013, A&A, 558, A33
Batalha, N. E., Marley, M. S., Lewis, N. K., & Fortney, J. J. 2019, ApJ, 878, 70
Batalha, N. 2019, natashabatalha/picaso: Initial Publication Release, v0.0, Zenodo, doi:10.5281/zenodo.2647593
Bean, J. L., Stevenson, K. B., Batalha, N. M., et al. 2018, PASP, 130, 114402
Bell, T. J., Nikolov, N., Cowan, N. B., et al. 2017, ApJL, 847, L2
Bradley, L., Sipőcz, B., Robitaille, T., et al. 2019, astropy/photutils: v0.6, Zenodo, doi:10.5281/zenodo.2533376
Carter, J. A., & Winn, J. N. 2009, ApJ, 704, 51
Chen, G., Casasayas-Barris, N., Pallé, E., et al. 2020, A&A, 635, A171
Chen, G., Guenther, E. W., Pallé, E., et al. 2017a, A&A, 600, A138
Chen, G., Pallé, E., Nortmann, L., et al. 2017b, A&A, 600, L11
Chen, G., Pallé, E., Welbanks, L., et al. 2018, A&A, 616, A145
Cubillos, P., Harrington, J., Loredo, T. J., et al. 2017, AJ, 153, 3
Demory, B.-O., de Wit, J., Lewis, N., et al. 2013, ApJL, 776, L25
Esteves, L. J., De Mooij, E. J. W., & Jayawardhana, R. 2015, ApJ, 804, 150
Evans, T. M., Pont, F., Sing, D. K., et al. 2013, ApJL, 772, L16
Feng, Y. K., Line, M. R., Fortney, J. J., et al. 2016, ApJ, 829, 52
Foreman-Mackey, D., Agol, E., Ambikasaran, S., & Angus, R. 2017, AJ, 154, 220
Foreman-Mackey, D., Luger, R., Czekala, I., et al. 2020, exoplanet-dev/exoplanet v0.4.3, Zenodo, doi:10.5281/zenodo.1998447
Gibson, N. P., Aigrain, S., Pont, F., et al. 2012a, MNRAS, 422, 753
Gibson, N. P., Aigrain, S., Roberts, S., et al. 2012b, MNRAS, 419, 2683
Haggard, H. M., & Cowan, N. B. 2018, MNRAS, 478, 371
Harris, C. R., Millman, K. J., van der Walt, S. J., et al. 2020, Natur, 585, 357
Hellier, C., Anderson, D. R., Collier Cameron, A., et al. 2011, A&A, 535, L7
Heng, K., & Demory, B.-O. 2013, ApJ, 777, 100
Hunter, J. D. 2007, CSE, 9, 90
Jansen, T., & Kipping, D. 2018, MNRAS, 478, 3025
Kataria, T., Showman, A. P., Fortney, J. J., et al. 2015, ApJ, 801, 86
Kataria, T., Showman, A. P., Fortney, J. J., Marley, M. S., & Freedman, R. S. 2014, ApJ, 785, 92
Keating, D., & Cowan, N. B. 2017, ApJL, 849, L5
Kenworthy, M. A., Mellon, S. N., Bailey, J. I., et al. 2021, A&A, 648, A15
Kreidberg, L. 2015, PASP, 127, 1161
Lewis, N. K., Wakeford, H. R., MacDonald, R. J., et al. 2020, ApJL, 902, L19
Luger, R., Agol, E., Foreman-Mackey, D., et al. 2019, AJ, 157, 64
Mandel, K., & Agol, E. 2002, ApJL, 580, L171
Marley, M. S., Ackerman, A. S., Cuzzi, J. N., & Kitzmann, D. 2013, in Comparative Climatology of Terrestrial Planets, ed. S. J. Mackwell et al. (Tucson, AZ: Univ. Arizona Press), 367
Marley, M. S., Gelino, C., Stephens, D., Lunine, J. I., & Freedman, R. 1999, ApJ, 513, 879
McKinney, W. 2010, in Proc. 9th Python in Science Conf., ed. S. van der Walt & J. Millman (Austin, TX: SciPy), 56
Morley, C. V., Fortney, J. J., Marley, M. S., et al. 2012, ApJ, 756, 172
Mullally, S. E., Rodriguez, D. R., Stevenson, K. B., & Wakeford, H. R. 2019, RNAAS, 3, 193
Nikolov, N., Sing, D. K., Burrows, A. S., et al. 2015, MNRAS, 447, 463
Niraula, P., Redfield, S., de Wit, J., et al. 2018, arXiv:1812.09227
Nortmann, L., Pallé, E., Murgas, F., et al. 2016, A&A, 594, A65
Nortmann, L., Pallé, E., Salz, M., et al. 2018, Sci, 362, 1388
Oreshenko, M., Heng, K., & Demory, B.-O. 2016, MNRAS, 457, 3420
Ormel, C. W., & Min, M. 2019, A&A, 622, A121
Palle, E., Chen, G., Prieto-Arranz, J., et al. 2017, A&A, 602, L15
Parmentier, V., Fortney, J. J., Showman, A. P., Morley, C., & Marley, M. S. 2016, ApJ, 828, 22
Pont, F., Zucker, S., & Queloz, D. 2006, MNRAS, 373, 231
Powell, D., Zhang, X., Gao, P., & Parmentier, V. 2018, ApJ, 860, 18
Salvatier, J., Wiecki, T. V., & Fonnesbeck, C. 2016, PeerJ Computer Science, 2, e55
Schöniger, A., Wöhling, T., Samaniego, L., & Nowak, W. 2014, WRR, 50, 9484
Schwartz, J. C., & Cowan, N. B. 2015, MNRAS, 449, 4192
Schwarz, G. 1978, AnSta, 6, 461
Shporer, A., & Hu, R. 2015, AJ, 150, 112
Sing, D. K., Fortney, J. J., Nikolov, N., et al. 2016, Natur, 529, 59
Spake, J. J., Sing, D. K., Evans, T. M., et al. 2018, Natur, 557, 68
Stevenson, K. B., Désert, J.-M., Line, M. R., et al. 2014, Sci, 346, 838
Stevenson, K. B., Line, M. R., Bean, J. L., et al. 2017, AJ, 153, 68
STScI Development Team 2013, pysynphot: Synthetic Photometry Software Package, Astrophysics Source Code Library, ascl:1303.023
Sudarsky, D., Burrows, A., & Pinto, P. 2000, ApJ, 538, 885
Theano Development Team 2016, arXiv:1605.02688
Thorngren, D., Gao, P., & Fortney, J. J. 2019, ApJL, 884, L6
Todorov, K. O., Désert, J.-M., Huitson, C. M., et al. 2019, A&A, 631, A169
Venot, O., Parmentier, V., Blecic, J., et al. 2020, ApJ, 890, 176
Virtanen, P., Gommers, R., Oliphant, T. E., et al. 2020, NatMe, 17, 261
von Essen, C., Mallonn, M., Hermansen, S., et al. 2020, A&A, 637, A76
von Essen, C., Ofir, A., Dreizler, S., et al. 2018, A&A, 615, A79
Wakeford, H. R., Sing, D. K., Stevenson, K. B., et al. 2020, AJ, 159, 204
Wakeford, H. R., Visscher, C., Lewis, N. K., et al. 2017, MNRAS, 464, 4247
Webber, M. W., Lewis, N. K., Marley, M., et al. 2015, ApJ, 804, 94